Cement & Concrete Composites 41 (2013) 45–59

Contents lists available at SciVerse ScienceDirect

Cement & Concrete Composites

journal homepage: www.elsevier.com/locate/cemconcomp

Lattice Discrete Particle Modeling (LDPM) of Alkali Silica Reaction (ASR) deterioration of concrete structures

Mohammed Alnaggar [a], Gianluca Cusatis [a,*], Giovanni Di Luzio [b]

[a] Department of Civil and Environmental Engineering, Northwestern University, Evanston, IL 60208, USA
[b] Department of Structural Engineering (DIS), Politecnico di Milano, Piazza Leonardo da Vinci 32, 20133 Milano, Italy

ARTICLE INFO

Article history:
Received 5 January 2013
Received in revised form 17 April 2013
Accepted 25 April 2013
Available online 4 May 2013

Keywords:
Alkali silica reaction
Concrete
Lattice model
Particle model
Cracking
Deterioration

ABSTRACT

A large number of structures especially in high humidity environments are endangered by Alkali–Silica Reaction (ASR). ASR leads to the formation of an expansive gel that imbibes water over time. The gel expansion causes cracking and consequent deterioration of concrete mechanical behavior in the form of strength and stiffness reduction. In the recent past, many research efforts were directed towards evaluation, modeling and treatment of ASR effects on structures but a comprehensive computational model is still lacking. In this paper, the ASR effect is implemented within the framework of the Lattice Discrete Particle Model (LDPM), which simulates concrete heterogeneous character at the scale of coarse aggregate pieces. The proposed formulation, entitled ASR-LDPM, allows precise and unique modeling of volumetric expansion; expansion anisotropy under applied load; non-uniform cracking distribution; concrete strength and stiffness degradation; alkali ion concentration effect; and temperature effects of concrete subjected to ASR. In addition, a unique advantage of this formulation is its ability to distinguish between the expansion directly related to ASR gel expansion and the one associated with cracking. Simulation of experimental data gathered from the literature demonstrates the ability of ASR-LDPM to predict accurately ASR-induced concrete deterioration.

1. Introduction

Deterioration induced by Alkali–Silica Reaction (ASR) is reported in many concrete structures all around the world, especially those built in high humidity and warm environments [1]. Water is essential for ASR to occur but, in addition, temperature plays a fundamental role in determining the ASR rate of reaction [2], namely the higher is the temperature the faster is the reaction. However, even in countries with average low temperatures ASR is reported to be a serious problem for the durability of concrete structures. The main effect of ASR is a progressive deterioration of concrete stiffness and strength that results from the long term formation and expansion of ASR gel inducing expansive pressure on the internal structure of concrete. This pressure causes nonuniform deformations that eventually lead to cracking and damage. While the chemical description of the reaction was addressed intensively in the literature, the fracture mechanics associated with the progressive expansion has received little attention due to the lack of models describing concrete internal structure satisfactorily. The main objective of the research reported in this paper is to fill this knowledge gap.

First reports on the effect of ASR on concrete structures are due to Stanton in 1940 [3]. This early research studied ASR chemistry; ASR effects at structure and material level; testing methods to investigate the vulnerability of aggregate and mixes to ASR; and techniques for the mitigation of ASR effects. The assessment of ASR effects has been pursued by several authors in a variety of different experimental programs [4–11,1]. Available ASR experimentation relies often on the analysis of ASR products through Scanning Electron Microscopy (SEM) and Energy-Dispersive X-ray (EDX) techniques [12–14]. For the experimental investigation of ASR in more realistic situations, accelerated ASR tests, such as the Accelerated Mortar Bar Test (AMBT) [15–17] and Concrete Prism Test (CPT) [18,19], are typically used.

Furthermore, in the past, various research efforts focused on studying the different factors affecting ASR, including, but not limited to, pessimum size (particle size associated with the maximum expansion over the test time period compared to both smaller and larger aggregate sizes), type of aggregate, temperature, relative humidity, and stress state [4,20–34]. Other research can be found on the mitigation of ASR problems by using either admixtures, especially fly ash [35–37], or remedial actions such as slot cutting or grouting of cracks [38].

* Corresponding author. Address: McCormick School of Engineering and Applied Science, Northwestern University, Tech Building Room A125, 2145 N Sheridan Rd., Evanston, IL 60208-3109, USA. Tel.: +1 (847) 491 4027.
E-mail addresses: MohammedAlnaggar2012@u.northwestern.edu (M. Alnaggar), g-cusatis@northwestern.edu (G. Cusatis), diluzio@stru.polimi.it (G.D. Luzio).

0958-9465/$ - see front matter © 2013 Elsevier Ltd. All rights reserved.
http://dx.doi.org/10.1016/j.cemconcomp.2013.04.015

From the modeling point of view, ASR simulation and its effect on concrete structures have been attempted at various length scales. Theoretical models describing ASR gel evolution based on petrographic measurements were proposed by several authors [39–41,21,42,22,43–45]. These models succeeded in capturing various aspects of ASR expansion such as aggregate pessimum size, ASR induced expansion and pressure but not the fracture mechanics aspects of the deterioration process. A fracture mechanics approach to predict the pessimum size of aggregate was proposed by Bažant [46].

In the literature, one can find macroscopic models trying to describe the global mechanical deterioration due to ASR. One of the earliest models was the phenomenological model presented by Charlwood et al. [47] and Thompson et al. [48]. More refined models [49] and others considering creep [50] were developed later and, although they predict well displacements and stress history in the structure, they completely lack the ability to predict crack patterns as well as to describe the physical phenomena linking ASR to the deterioration of mechanical properties.

Another improvement in macroscopic models was obtained by the formulation of chemo-mechanical coupled models. Huang and Pietruszczak [51,52] and Ulm et al. [53] developed models based on the ASR kinetics. The latter approach, implemented within smeared crack finite element frameworks [54,55], was able to reproduce some ASR expansion data available in the literature [56].

Models considering stress state effects have been also developed. Among others, it is worth mentioning the model by Saouma and Perotti [57] and Multon et al. [58]. Damage models combining in a consistent thermodynamic fashion the chemical and mechanical components of the ASR process were considered by Comi et al. [59,60]. The effect of humidity and temperature was incorporated in the reaction kinetics law by Poyet et al. [61]. While all previous models were deterministic, Capra and Sellier [62] presented a probabilistic model based on the main parameters of ASR and concrete. For very extensive literature reviews of available ASR models, the reader may want to consult Refs. [63] and [2].

Despite some success, the common disadvantage of all aforementioned models is the inability to simulate crack patterns and crack distribution due to ASR. This, in turn, limits the ability to predict the degradation effect of ASR and forces the assumption of phenomenological relationships between ASR gel expansion and concrete mechanical properties. In addition, it also limits the ability of such models to explain complex triaxial behavior of concrete under ASR and also forces the assumption of phenomenological relationships between ASR gel expansion and stress state. These limitations are inherently connected to modeling concrete as an isotropic and homogenous continuum.

Due to lack of reliable mini scale or meso scale models – describing concrete as a three-phase (aggregate, binder, interfacial transition zone) or two-phase (aggregate, binder) material, respectively – very limited results are available on fine scale modeling of cracking induced by ASR. Comby-Peyrot et al. [64] developed a 3D computational tool to describe concrete behavior at mesoscale with the application to ASR. The model predicted well concrete nonlinear behavior up to the peak but was unable to reproduce complete degradation in the softening regime. Dunant et al. [65] proposed a 2D model able to qualitatively reproduce material deterioration of concrete properties by simulating expansive gel pockets inside the aggregates. The 2D character of the model, however, prevented the model from obtaining good results from a quantitative point of view. Shin and colleagues [66,67] used scanning electron microscopy techniques to obtain microstructural images of specimens suffering from ASR and to develop refined, and computationally very intensive, 2D finite element models of damaged internal structure of concrete.

In this paper, all aforementioned limitations are overcome by modeling ASR effects within the Lattice Discrete Particle Model (LDPM) [68,69,91,92]. LDPM, in a full 3D setting, simulates the mechanical interaction of coarse aggregate pieces through a system of three-dimensional polyhedral particles, each resembling a spherical coarse aggregate piece with its surrounding mortar, connected through lattice struts [68] and it has the ability of simulating the effect of material heterogeneity of the fracture processes [69]. ASR-LDPM introduced here is limited to fully saturated conditions as the consideration of water macro diffusion is out of the scope of this paper and will be considered in future work.

2. Alkali Silica Reaction (ASR) modeling

According to the model proposed by Bažant and Steffens [21] – adopted and extended in this section – the overall ASR process can be approximately described by considering that (1) water needs to be available in the pores to act as transport medium for hydroxyl and alkali ions for ASR to occur; (2) the expansion of ASR gel is mostly due to water imbibition; and (3) a continuous supply of water is needed for the swelling to continue over time. As in the original model and consistently with the LDPM formulation, the aggregate particles are assumed to have spherical shape; the whole volume of each particle is assumed to be reactive; and the silica is assumed to be smeared uniformly over each aggregate volume. This is certainly an approximation compared to reality in which shape and size of the aggregate particles may vary widely, as well as the content of reactive silica in flaws, inclusions, and veins. Under this approximation, however, the dissolution of silica may be assumed to progress roughly in a uniform manner in the radial direction inward from the surface towards the particle center. In addition, ASR continues as long as water is continuously provided by macro-diffusion processes. For low values of relative humidity (<60–80%) ASR slows down and eventually stops [70]. However, in this study, only saturation condition is considered. This case has practical relevance in situations in which concrete is continuously exposed to water as, for example, for dams and offshore structures.

2.1. Gel formation

Thermodynamics and kinetics of the ASR reaction were studied in Refs. [71,72] and it was concluded that the chemical reaction rate is much faster than the actual rate of ASR production observed in concrete structures. This led researchers to the conclusion that some other mechanism had to be the dominant one and it was observed that as the reaction progresses, the unreacted silica in the interior of each of aggregate particle is shielded by a spherical layer of the reaction product, the ASR gel. Through this layer further water molecules must diffuse in order to reach the reacting surface of the particle and dissolve more silica. This diffusion slows down the ASR tremendously and becomes the process governing the rate of ASR [71,72]. In comparison the chemical reaction at the silica dissolution front may be considered to be almost instantaneous. Thus, the rate of ASR gel production can be best approximated by solving a diffusion problem.

Consistently, for a steady state diffusion process at constant temperature, one can write [21]

$$M_w = w_s \frac{1 - z/x}{1 - 2z/D} \tag{1}$$

where M_w= water concentration within the layer of ASR gel; x = radial coordinate; z = radius of the remaining unreacted particle; and D = aggregate particle diameter (See Fig. 1a for details). In addition, w_s is the concentration of water in the concrete surrounding the

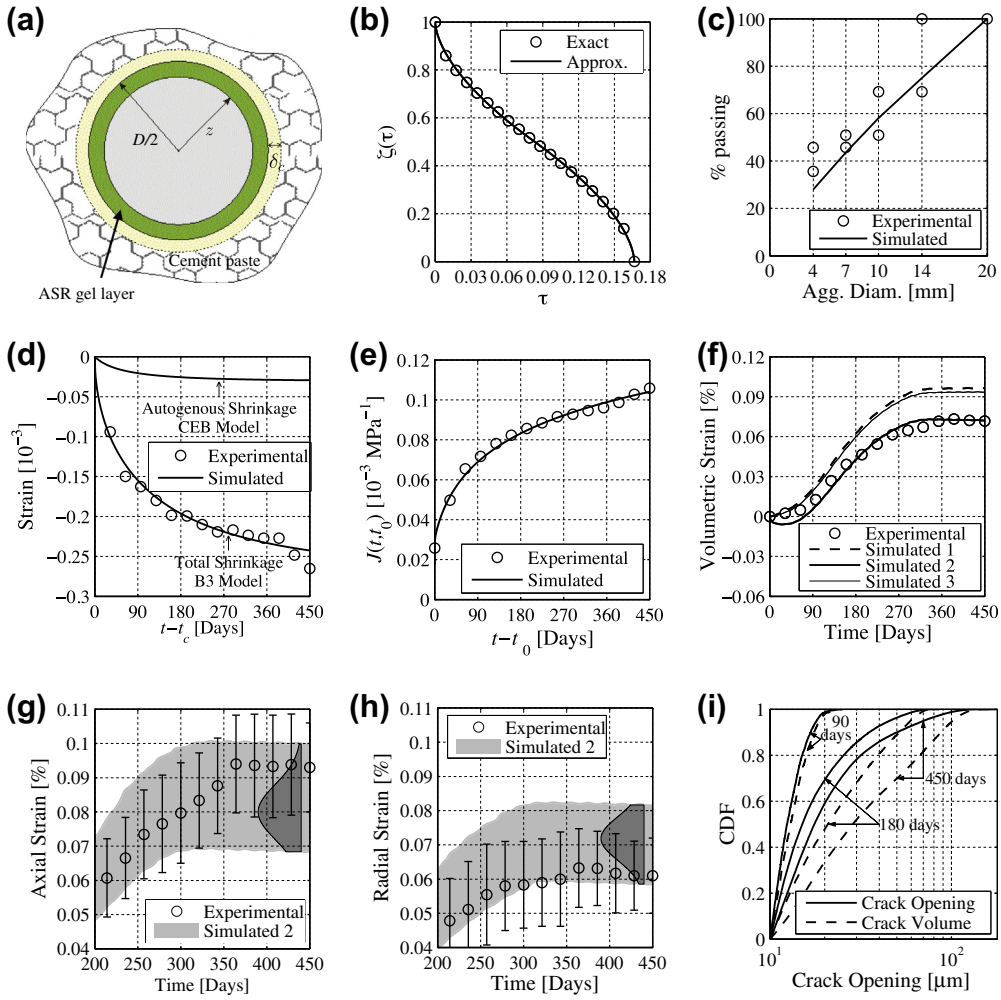

Fig. 1. (a) Idealization of gel formation in one aggregate. (b) Exact and approximate solutions for Eq. (4). (c) Simulated and experimental sieve curve for data from Ref. [26]. (d) Simulated autogeous shrinkage with CEB model, simulated total shrinkage with B3 model' and reported experimental shrinkage. (e) Fitting of compliance function for creep using B3 model. (f) Volumetric strain evolution for the unrestrained free expansion case. (g) Axial strains for 20 simulated specimens. (h) Radial strains for 20 simulated specimens, and i) CDFs for crack opening and volume for one specimen at 90, 180 and 450 days.

aggregate particle and can be estimated [73,93], as $w_s = (w/c - 0.188\alpha_c^\infty)c$; $\alpha_c^\infty = (1.031\ w/c)/(0.194 + w/c)$ (asymptotic hydration degree); w/c = water-to-cement ratio; c = cement content.

Furthermore, the advancement of the reaction front can be expressed through a mass balance equation expressing the balance between the water available and the water used in the chemical reaction:

$$r_w c_s\ \mathrm{d}z = -a_s(T)\frac{\partial M_w}{\partial x}\bigg|_{x=z}\mathrm{d}t \tag{2}$$

in which t = time; r_w = water-to-silica stoichiometric ratio; c_s = silica content, e.i. mass of silica per unit volume of aggregate; and $a_s(T)$ = temperature dependent ASR gel permeability to water. The silica content varies based on the aggregate type; it can be as high as about 50% of the aggregate volume and its average value can be estimated in about 20% [74]. Considering that the silica mass density is 2200 kg/m^3, one can assume, in absence of more accurate information, $c_s \approx 440$ kg/m^3.

A stoichiometric relationship for the ASR reaction is very difficult to ascertain due to the great variety of possible chemical equilibria for different values of pH [71,72,75,76]. In this study, as also done in [21], the monomer $H_2SiO_4^-$ is considered to be the main form of basic gel produced by the dissolution process. In this case, it can be stated that about two water molecules are necessary to dissolve one silica atom and one can set $r_w = 2m_w/m_s$; m_w = 18 g/mole; and m_s=60.09 g/mole.

The temperature dependence of the permeability can be formulated with an Arrhenius-type equation [77,78,73] as

$$a_s(T) = a_{s0}\ \exp\left(\frac{E_{ad}}{RT_0} - \frac{E_{ad}}{RT}\right) \tag{3}$$

where a_{s0} = permeability at the reference temperature T_0; T = current temperature; E_{ad} = activation energy of the diffusion process; and R = universal gas constant. It is worth observing that Eq. (3) can be assumed to apply to practical applications, in which temperature is not actually constant in time, because, for normal operation of typical concrete structures, the time scale of temperature variations (days for night/day variations; and months for seasonal variations) are much shorter than the time scale of the progression of ASR (from years to decades).

Substituting Eq. (1) into Eq. (2), one obtains

$$\frac{\mathrm{d}\zeta}{\mathrm{d}\tau} = -[\zeta(1-\zeta)]^{-1} \tag{4}$$

where $\tau_s = 0.25D^2/a_s(T)$; $k_s = w_s/r_w c_s$; $\tau = t\ k_s/\tau_s$, non-dimensional reaction time; and $\zeta = 2z/D$, non-dimensional reaction front position.

Integration of Eq. (4) with the initial condition $\tau = 0$, $\zeta = 1$ results in $\tau(\zeta) = 1/6 - \zeta^2/2 + \zeta^3/3$. It is easy to verify that the reaction front reaches halfway the particle radius, $\zeta = 0.5$, and the center of the particle (full reaction), $\zeta = 0$, for $\tau = 1/12$ and $\tau = 1/6$, respectively. Although it is possible to calculate analytically $\zeta(\tau)$ from $\tau(\zeta)$, it is convenient to approximate the exact solution as $\zeta(\tau) = 1 - \kappa_m \tau^m$ for $0 \leqslant \tau \leqslant 1/12$, and $\zeta(\tau) = \kappa_m(1/6 - \tau)^m$ for $1/12 < \tau \leqslant 1/6$ with $\kappa_m = 12^m/2$. For $m = 0.6$ (Fig. 1b) the aforementioned approximation is characterized by a maximum error smaller than 1.3%.

For any calculated value of the reaction front position, the total mass of basic gel, M_g, produced in one aggregate particle of diameter D, can be determined by multiplying the volume of silica in the reacted volume of aggregate by the silica-to-gel conversion ratio, m_g/m_s. One can write

$$M_g = \kappa_a \frac{\pi D^3}{6}(1 - \zeta^3) c_s \frac{m_g}{m_s} \tag{5}$$

where $m_g = 94.1$ g/mol. In Eq. (5), the factor κ_a accounts for the fact that alkali content available in the cement paste surrounding each aggregate particle, is not always enough for the ASR reaction to occur. In other words, the discussed availability of water at reaction front is not a sufficient condition for ASR and such water needs to be alkali rich. In this study, in absence of more detailed information, a simple linear relationship between alkali content, c_a, and the produced gel mass is assumed: $\kappa_a = \min\left(\langle c_a - c_a^0\rangle/(c_a^1 - c_a^0), 1\right)$, where c_a^0 is the threshold alkali content at which, no or minimal expansion is observed, and c_a^1 is the saturation alkali content enough for complete silica reaction.

2.2. Water imbibed by ASR gel

The ASR product is a gel, which has the capacity – typical of colloidal systems – to imbibe water molecules, causing extensive swelling [79]. Since the ASR gel is constrained in the pores of concrete, the swelling produces pressure in the gel and the surrounding concrete structure and lead to cracking and damage. Expansion of the ASR gel can be partly accommodated without significant pressure build up by filling the capillary pores in the hardened cement paste located close to the surface of the reactive aggregate particles. This is also facilitated by the existence of the so-called interfacial transition zone (ITZ) that is a layer of material with higher porosity in the hardened cement paste near the aggregate surface. Similarly to the ITZ size, the thickness, δ_c, of the layer in which the capillary pores are accessible to the ASR gel may be considered constant and independent of the particle size D.

As already mentioned, the physical properties of the basic form of ASR gel are not yet known completely. But it seems reasonable to assume that the formation of gel causes no significant volume increase "per se" and that all volume changes are caused solely by the intake of additional water.

The imbibition of water from the bulk of mortar or concrete into the gel cannot happen instantly, but it is the result of a local microdiffusion process that occurs with some delay. However, since the gel is partly expelled into the pores around each aggregate particle, the geometry of this diffusion process is not spherical and it appears difficult to choose any particular idealized geometry. Therefore similarly to Ref. [21], it seems more appropriate to conduct merely a simplified overall analysis in which one postulates that the evolution in time of the imbibed water is governed by the following equation: $\dot{M}_i = A_i/\tau_i$, where M_i= mass of water imbibed by the basic gel; A_i = thermodynamic affinity (thermodynamic driving force) of the imbibition process; and τ_i = characteristic imbibition time. A simple expression for A_i can be obtained assuming that the driving force of water imbibition is the imbalance between the imbibed water at thermodynamic equilibrium and the current imbibed water:

$$A_i = \kappa_i^0 \exp\left(\frac{E_{ai}}{RT_0} - \frac{E_{ai}}{RT}\right) M_g - M_i \tag{6}$$

where the imbibed water at thermodynamic equilibrium has been assumed to be proportional to the mass of formed gel and temperature-dependent through an Arrhenius-type equation governed by the activation energy of the imbibition process, E_{ai}.

For reasons of dimensionality, the characteristic time of the imbibition process, can be expressed as $\tau_i = \delta^2/C_i$, in which C_i is the diffusivity for microdiffusion of water close to the aggregate (surely much lower than the diffusivity for global water diffusion through a concrete structure), δ is the average (or effective) distance of water transport process from the concrete around the aggregate into the ASR gel, and $\eta(M_i)$ is an increasing function of M_i. For two adjacent aggregate particles of diameters D_1 and D_2, δ can be estimated as $\delta = (\ell - D_1 - D_2)/2$, where ℓ is the distance between the particle centers. Furthermore, it is reasonable to consider the micro-diffusivity C_i to be a decreasing function of M_i, because the imbibition of the layers of gel increases the diffusion time of the free water to reach the not imbibed gel. This phenomenon can be captured by setting $C_i = C_i^0 \exp(-\eta M_i)$.

By considering all these effects together and taking into account Eq. (5), one can finally obtain the governing equation for water imbibition into the gel

$$\dot{M}_i = \frac{C_i^0}{\delta^2} \exp(-\eta M_i)\left[K_i^0 (1 - \zeta^3) D^3 \kappa_a \exp\left(\frac{E_{ai}}{RT_0} - \frac{E_{ai}}{RT}\right) - M_i\right] \tag{7}$$

where $K_i^0 = \pi \kappa_i^0 c_s m_g/(6 m_s)$. Analysis of experimental data carried out in this study suggests that, in absence of more precise information about the water imbibition process, $\kappa_i^0 \approx 1$ for $T_0 = 23\ ^\circ\text{C} = 296$ K is a reasonable assumption. This, along with an average value for c_s (see Section 2.1) gives $K_i^0 = 360.777$ kg/m^3

Finally, from the mass of imbibed water the gel volume variation can be calculated as $\Delta V_g = M_i/\rho_w$ with $\rho_w = 1000$ kg/m^3.

3. Lattice discrete particle modeling of ASR effects

The Lattice Discrete Particle Model (LDPM) formulated, calibrated, and validated by Cusatis and coworkers [68,69], is a meso-scale discrete model that simulates the mechanical interaction of coarse aggregate pieces. Concrete mesostructure is constructed through the following steps. (1) The coarse aggregate pieces, whose shapes are assumed to be spherical, are introduced into the concrete volume by a try-and-reject random procedure. (2) Zero-radius aggregate pieces (nodes) are randomly distributed over the external surfaces to facilitate the application of boundary conditions. (3) A three-dimensional domain tessellation, based on the Delaunay tetrahedralization of the generated aggregate centers, creates a system of polyhedral cells interacting through triangular facets and a lattice system composed by the line segments connecting the particle centers.

In LDPM, particle rigid body kinematics is used to describe the deformation of the lattice/particle system and the displacement jump, $[\![\mathbf{u}_C]\!]$, at the centroid of each facet is used to define measures of strain as

$$e_N = \frac{\mathbf{n}^T [\![\mathbf{u}_C]\!]}{\ell}; \quad e_L = \frac{\mathbf{l}^T [\![\mathbf{u}_C]\!]}{\ell}; \quad e_M = \frac{\mathbf{m}^T [\![\mathbf{u}_C]\!]}{\ell} \tag{8}$$

where ℓ = interparticle distance; and $\mathbf{n}$, $\mathbf{l}$, and $\mathbf{m}$, are unit vectors defining a local system of reference attached to each facet.

Next, a vectorial constitutive law governing the behavior of the material is imposed at the centroid of each facet. In the elastic regime, the normal and shear stresses are proportional to the corre-

sponding strains: $t_N = E_N e_N$; $t_M = E_T e_M$; $t_L = E_T e_L$, where $E_N = E_0$, $E_T = \alpha E_0$, E_0= effective normal modulus, and α = shear-normal coupling parameter. In the inelastic regime, a nonlinear constitutive equation is used to describe meso-scale failure phenomena such as fracturing and shearing; frictional behavior; and pore collapse under high compressive stresses. Detailed description of model behavior in the nonlinear range can be found in Ref. [68] and is summarized in Appendix A. Finally, the governing equations of the LDPM framework are completed through the equilibrium equations of each individual particle.

To account for ASR in LDPM, first the radius variation of each aggregate particle of initial radius $r = D/2$ can be calculated from the volume variation of the ASR gel due to water imbibition:

$$\Delta r = \left(\frac{3M_i}{4\pi\rho_w} + r^3\right)^{1/3} - r \tag{9}$$

This result can be then used to calculate an incompatible ASR strain, e_N^0, to be applied to the LDPM system assuming that strain additivity holds:

$$e_N = e_N^t + e_N^0 \tag{10}$$

where $e_N^0 = (\Delta r_1 + \Delta r_2 - \delta_c)/\ell$; Δr_1 and Δr_2 are the radius changes of the two aggregate particles sharing a generic facet; and e_N^t is the stress-dependent normal strain calculated according to the LDPM constitutive equation. Note that the model formulated herein assumes approximately that the imposed facet shear strains due to gel swelling are negligible, $e_M^0 = e_L^0 \approx 0$, although this might not be exactly true due to the irregular shape of actual aggregate particles.In addition, the increments of the radius variations are set to zero after full reaction of the relevant aggregate particles since, at this stage, it can be arguably assumed that additional gel expansion can be accommodated into the empty spaces produced by cracking occurring both inside the aggregate particles and in the close proximity of the aggreagate surface.

The proposed model can also capture the effect of pessimum aggregate size, which is typically defined as the aggregate size that causes the maximum expansion during a fixed time interval [27,30]. For aggregate particles smaller than the pessimum size, the reduced expansion is due to the fact that most of the gel expansion is accommodated by the ITZ porosity. The current formulation accounts for this phenomenon through the parameter δ_c discussed previously. For aggregate particles larger than the pessimum size, the reduced expansion is only due to the fact that the expansion is measured within a constant time window. Larger aggregate require more time to fully react as the reaction process is slowed down by the diffusion of water through the ASR gel.

By solving Eq. (10) for e_N^t the LDPM facet stresses can be calculated. In the elastic regime, one obtains, $t_N = E_N(e_N - e_N^0)$; $t_M = E_T e_M$; and $t_L = E_T e_L$. Similar equations can be obtained in the more general inelastic case.

It is important to observe that the proposed formulation does not postulate any stress dependence of gel volume formation and swelling. Such dependence has been advocated by some authors [80,81,26] in the literature to explain the experimental data dealing with specimens experiencing ASR with and without applied loads and showing distinctly different ASR macroscopic expansion. As it will be discussed later in this paper, the proposed formulation is able to simulate such differences simply by accounting for meso-scale cracking and the effect of applied load on cracking. This is possible within the LDPM framework due to the intrinsic ability to simulate material heterogeneity and its effect on concrete mechanical response.

The presented formulation, entitled ASR-LDPM, is implemented into MARS, a multi-purpose computational code for the explicit dynamic simulation of structural performance [82].

4. Identification of model parameters

The proposed model contains two sets of material parameters that need to be identified from experimental data. The first set consists of the LDPM parameters which can be identified through fitting material properties relevant to basic concrete mechanical behavior. Extensive discussion of LDPM parameter calibration is reported in Ref. [69] to which the reader is directed for additional information.

The second set of material parameters is relevant to the formulated ASR model. The ASR parameters can be calibrated by the best fitting of volume expansion versus time curves of concrete specimens subject to ASR (1) at the reference temperature T_0 (typically room temperature) and with an alkali content $c_a > c_a^1$ sufficient for the complete reaction of all reactive aggregate particles in the concrete mix, for a_{s0}, C_i^0, η, and δ_c; (2) at two different temperatures, for the activation energies of gel formation, E_{ad}, and water imbibition, E_{ai}; and (3) at two alkali content values, for the saturation and threshold alkali contents, c_a^1 and c_a^0.

It is worth mentioning that, due to the intrinsic randomness of both experimental data and LDPM numerical response, the parameter identification needs to be performed by averaging the response of a statistically representative number N of specimens. In this study, unless otherwise mentioned, $N = 3$ was used when the relevant information was not available from the experiments.

5. Numerical simulations and comparison with experimental data

This section presents the numerical simulation of ASR induced expansion of concrete specimens with the objective of demonstrating the capability of the formulated model to capture (1) the general characteristics of ASR S-shaped expansion versus time curves; (2) the effect of stress states on observed expansion; (3) the effect of expansion on concrete strength; (4) the effect of alkali content; and (5) the effect of temperature.

5.1. Free and restrained ASR expansion under different applied loads

To verify the ability of the model to predict correctly ASR-induced expansion under different loading conditions, this section presents the simulation of experimental results obtained by Multon and Toutlemonde [26]. Experiments were performed using sealed cylindrical specimens (240 mm length and 130 mm in diameter). Three different cases were considered: (1) free expansion; (2) restrained expansion by using a 3 mm and thick steel ring; and (3) restrained expansion by using a 5 mm thick steel ring. For each case three loading conditions were considered and consisted in axial stresses of 0, 10, and 20 MPa. The tests were characterized by a duration of 450 days after curing the specimens for 28 days at room temperature. Axial strains corresponding to the total expansion of specimens were averaged from 14 measurements regularly spaced over the perimeter, while for radial strains, diameter variations were measured at three levels of the cylinders, at 10 regularly spaced angular locations.

This data concerns accelerated experiments, which, however, have been demonstrated to produce good representation of the actual long term phenomena [26,53], and macroscopic behaviors such as S-shaped expansion curves and stress effect in agreement with the corresponding values observed in actual applications.

5.1.1. Calibration of LDPM concrete parameters and creep, shrinkage considerations

To match concrete mechanical properties relevant to the analyzed experimental data, LDPM parameters were calibrated

based on reported values of compressive strength, $f'_c = 38.4$ MPa, Young's modulus, $E = 37.3$ GPa using cylindrical specimens 320 mm in height and 160 mm in diameter, and splitting tensile strength, $f'_t = 3.2$ MPa using cylindrical specimens 220 mm in height and 110 mm in diameter. Four numerical specimens (same number as in the experiments) with different meso-structures were simulated and their average response was considered. The generation of the different LDPM meso-structures was performed considering the grain size distribution reported in Fig. 1c (minimum aggregate size, $d_0 = 4$ mm; maximum aggregate size, $d_a = 20$ mm; fuller curve exponent, $n_F = 0.79$) and the following mix composition: cement content, $c = 410$ kg/m^3; water-to-cement ratio, $w/c = 0.5207$; aggregate-to-cement ratio, $a/c = 4.249$.

The identified or assumed (for lack of specific experimental data) LDPM parameters [68,69] are as follows: meso-scale normal modulus, $E_0 = 62{,}346$ MPa; densification ratio, $E_d/E_0 = 1$; shear-normal coupling parameter, $\alpha = 0.25$; meso-scale tensile strength, $\sigma_t = 4.75$ MPa; meso-scale compressive strength, $\sigma_{c0} = 150$ MPa; shear strength ratio, $\sigma_s/\sigma_t = 3.07$; meso-scale tensile characteristic length, $l_t = 75$ mm; softening exponent, $n_t = 0.2$; initial hardening modulus ratio, $H_{c0}/E_0 = 0.4$; transitional strain ratio, $\kappa_{c0} = 2$; initial friction, $\mu_0 = 0.2$; asymptotic friction, $\mu_\infty = 0$; transitional stress $\sigma_{N0} = 600$ MPa; deviatoric strain threshold ratio, $\kappa_{c1} = 1$; deviatoric damage parameter, $\kappa_{c2} = 5$. Using these parameters, the average of the simulated concrete properties are: $f'_{c,num} = 38.41$ MPa, $E_{num} = 37.7$ GPa, and $f'_{t,num} = 3.19$ MPa, which match the given experimental data with an error smaller than 0.026%, 1.07%, and 0.31%, respectively.

The experimental results analyzed in this section show, for the control nonreactive specimens, shrinkage of about 0.25%. Also for the loaded cases, experiments show a considerable amount of creep for applied loads of 10 MPa and 20 MPa. This is due to the relatively early age of the tested concrete. The meso-scale formulation presented in this paper does not include shrinkage and/or creep as it is meant to simulate long term ASR deterioration in concrete structures. In practical situations, when ASR effects are important (for relatively old structures) shrinkage/creep effects are most of time negligible.

In order to be able to simulate creep and shrinkage effects in the analyzed data set, a simplified approach was taken by adding basic creep and shrinkage strains macroscopically to the LDPM averaged response of the simulated specimens. More specifically, with reference to a cylindrical specimen subject to a macroscopic stress $\boldsymbol{\sigma}(t)$ composed of averaged axial stress component, $\sigma_a(t)$, and radial stress component, $\sigma_r(t)$, the corresponding macroscopic strain was calculated as $\boldsymbol{\varepsilon} = \boldsymbol{\varepsilon}^{LDPM} + \boldsymbol{\varepsilon}^{sh} + \boldsymbol{\varepsilon}^{ve}$; where $\boldsymbol{\varepsilon}^{LDPM}$, $\boldsymbol{\varepsilon}^{sh}$, and $\boldsymbol{\varepsilon}^{ve}$ are averaged macroscopic LDPM strain, shrinkage strain, and viscoelastic strain, respectively.

In the experimental campaign, the specimens were supposed to be sealed at all time and tested at 28 days of age. In this situation, the sole source of shrinkage should be the consumption of water due to hydration (autogenous shrinkage). However, comparison (see Fig. 1d) of shrinkage strain measured on companion non-reactive specimens and autogenous shrinkage strain estimated according to the CEB model [83], $\boldsymbol{\varepsilon}^{sh}_{au}(t) = -\varepsilon_\infty\left(1 - \exp[-0.2(t/t_0)^{0.5}]\right)\boldsymbol{I}$, $\boldsymbol{I} = [11]^T$, $t_0 = 1$ day, t = time in days and, $\varepsilon_\infty = 8.791 \times 10^{-5}$, shows a significant difference suggesting a potential occurrence of drying due to imperfect sealing of the specimens. This is further verified by fitting the experimental shrinkage data with the B3 model [84], $\boldsymbol{\varepsilon}^{sh}(t, t_c) = -C_h \tanh\sqrt{(t - t_c)/\tau_{sh}}\boldsymbol{I}$, $t_c = 28$ days. The best fitting, shown in Fig. 1d, leads to the following parameters: $\tau_{sh} = 213.7$ days and $C_h = 2.7075 \times 10^{-4}$, from which an average relative humidity of 91% can be then estimated. This value is lower than the value, 95 to 98%, typically reported for sealed specimens of standard concrete.

The viscoelastic strain can be calculated as $\boldsymbol{\varepsilon}^{ve} = C(t, t_0)\boldsymbol{G}\boldsymbol{\sigma}_0 + \int_{t_0}^{t} C(t, \tau)\,\boldsymbol{G}\dot{\boldsymbol{\sigma}}(\tau)\mathrm{d}\tau$ where $C(t,t_0) = J(t,t_0) - 1/E$; $J(t,t_0)$=compliance function; $G_{11} = 1$; $G_{12} = -2v$; $G_{21} = -v$; and $G_{22} = 1 - v$; $v = 0.17$, Poisson's ratio; and, according to the B3 model [84], $J(t,t_0) = q_1 + q_2 Q(t,t_0) + q_3 \ln[1 + (t - t_0)^n] + q_4 \ln(t/t_0)$.

Fitting of creep data (see Fig. 1e) leads to $q_1 = 1.758 \times 10^{-5}$ MPa^{-1}; $q_2 = 8.414 \times 10^{-5}$ MPa^{-1}; $q_3 = 1.794 \times 10^{-6}$ MPa^{-1}; and $q_4 = 2.46 \times 10^{-5}$ MPa^{-1}.

In the following sections, a complete analysis of model calibration and validation is presented through the comparison of experimental data and numerical simulations obtained by (1) excluding the effect of creep and shrinkage (curves labeled "Simulated 1"); (2) including creep and total shrinkage calibrated on companion specimen data (curves labeled "Simulated 2"); and (3) including creep and estimated autogenous shrinkage (curves labeled "Simulated 3").

5.1.2. Calibration of ASR parameters with free expansion data

The analyzed experiments are relevant to (1) an accelerated reaction, 450 days compared to 5–50 years in actual structures; (2) a mix design with a large fraction of reactive aggregate, all aggregate particles 4 mm in diameter and above were reactive (e.i. 64.5% of total aggregate content by weight); and (3) a cement type with high alkali content ($c_a > c^1_a$, $\kappa_a = 1$). Under these conditions it is likely that all pores surrounding each reactive aggregate surface were filled quickly with ASR products in the early 28 days of curing. In this case, it is reasonable to assume $\delta_c = 0$. In addition, since the experimental data did not contain information on temperature effect, the reference temperature T_0 was assumed to be equal to the room temperature (23 °C = 296 K) at which the experiments were carried out.

The remaining parameters ($a_{s0} = 1.478 \times 10^{-10}$ m^2/day, $C^0_i = 1.44 \times 10^{-14}$ m^2/day, $\eta = 36{,}813$ kg^{-1}) were calibrated by fitting the experimentally measured evolution in time of the volumetric strain, $(\varepsilon_a + 2\varepsilon_r)/3$, with the average LDPM response. The parameter optimization was performed through a nonlinear least square minimization procedure with reference to the Simulated 2 numerical response and the obtained fitting is shown in Fig. 1f. In the same figure, the Simulated 1 and Simulated 3 curves are also reported for comparison. As one can see the effect of shrinkage is not negligible and accounts for a reduced measured expansion of about 24% at 450 days. In the first 90 days, the LDPM calculated expansion is overcorrected by the shrinkage effect and the overall net strain is negative while, in the experiments, only positive strain (expansion) is observed. The Simulated 3 curve fits better the data in that time range suggesting that degradation of specimen sealing likely occurred overtime.

For this calibration, since the specimen is unrestrained, the macroscopic averaged stresses are zero and, consequently, there is no effect of creep in the numerical simulations. It must be observed that this is only an approximation because, in reality, creep might still occur in the internal heterogeneous structure of the material. This could be simulated by a creep formulation at the meso-scale but, as mentioned, earlier in this paper, this is outside the scope of the present work.

The response of the reactive unrestrained specimens is further analyzed in Fig. 1g and h showing separately axial and radial strains, respectively, including their scatter (in terms of maximum and minimum bounds) for both numerical and experimental data. As one can see the experimental axial and radial expansion are 0.093% and 0.061%, respectively, at 450 days, suggesting a somewhat anisotropic behavior under free expansion. This behavior, also observed by other authors [26,62], can have three distinct sources: (1) the number of tested specimens is too small to provide statistically accurate results; (2) a non-isotropic aggregate particle

distribution due to size and shape of the adopted specimens; and (3) the pouring direction during casting.

In Fig. 1g and h, the numerical results, which account automatically only for the first and second possible sources of deviation from the isotropic expansive behavior, are relevant to 20 different specimens as opposed to the experimental 4. Results show that the numerical scatter is comparable to the experimental one. However, the average numerical response is anisotropic but with a reduced anisotropy: the axial strain is 0.0800% and the radial strain is 0.0719% at 450 days. Furthermore, the average response of sets composed by 4 specimens within the 20 ranges from 0.0702% to 0.0918% for axial strain which is −12.30% to 14.72% compared with the average response of the entire set; and for radial strain, it ranges from 0.0615% to 0.792% which is −14.52% to 10.11% compared with the average response of the entire set. This discussion shows that although the number of specimens in the experimental campaign was somewhat limited from a statistical point of view, some other effect must be present to fully account for the anisotropic behavior.

The issue of size and shape of the specimens was also investigated in the numerical simulations by simulating 20 additional cubic specimens with side equal to the length of the tested cylinders (240 mm). Visual inspection of the generated particle distributions did show a more uniform particle distribution in the case of cubic specimens and less "wall effect" (absence of large aggregate particles near the boundaries). In this case, the average expansion strains are basically the same (from 0.1135% to 0.1148%) while their scatter ranges from 0.0988% to 0.1412%. Based on this discussion, the reduced expansion in the radial direction in the simulated response relevant to the averaged 20 specimens can be explained by wall effect.

Finally, Fig. 1i reports the Cumulative Distribution Function (CDF) for the calculated crack openings as well as crack volumes (crack opening × facet area) for three different ASR duration. The crack opening is defined as $w = \left(w_N^2 + w_M^2 + w_L^2\right)^{1/2}$, where $w_N = \ell\,(e_N - t_N/E_N)$,$w_M = \ell\,(e_M - t_M/E_T)$ and $w_L = \ell\,(e_L - t_L/E_T)$. A minimum threshold of 10 μm, corresponding to a local loss of carrying capacity of about 3–5%, was chosen to generate the CDFs. The maximum calculated crack width is about 25 μm at 90 days, 85 μm at 180 days and 180 μm at 450 days. These values agree well with typical values reported in the literature for similar concrete mixes [1]. It is interesting to observe that cracks visible by naked eyes (>100 μm) occur only after 200 days. This means that, if it is required to early detect ASR occurrence in real concrete structures, the use of only visual inspection is not sufficient as it will only detect ASR crack openings >100 μm while actually a large volume of cracking is happening below this threshold. It must observed that, as will be shown later, at 200 days the loss of carrying capacity is already about 25%. It should be noted that 200 days corresponds to 45% of the total 450 days of these accelerated expansion tests,

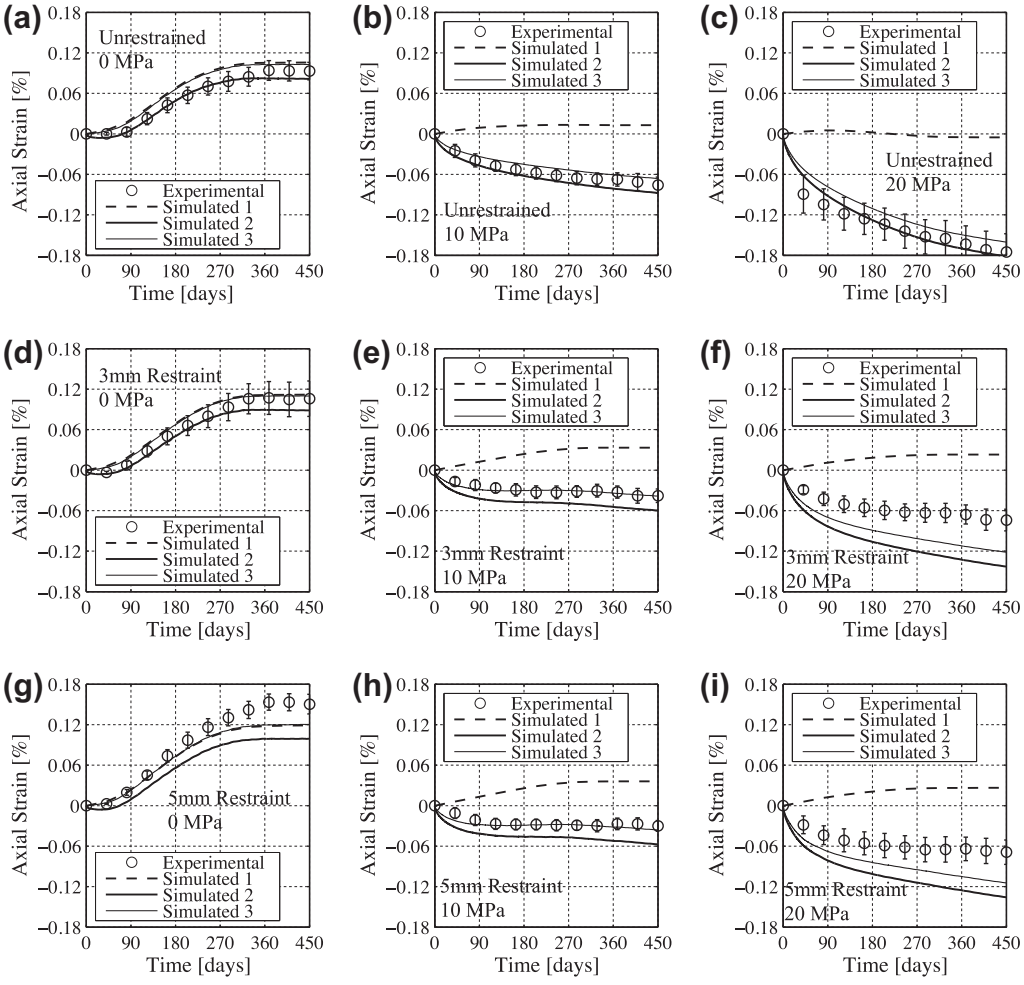

Fig. 2. Axial strain evolution for: (a) Unrestrained specimens under 0 MPa, (b) Unrestrained specimens under 10 MPa, (c) Unrestrained specimens under 20 MPa, (d) 3-mm-Restrained specimens under 0 MPa, (e) 3-mm-Restrained specimens under 10 MPa, (f) 3-mm-Restrained specimens under 20 MPa, (g) 5-mm-Restrained specimens under 0 MPa, (h) 5-mm-Restrained specimens under 10 MPa, (i) 5-mm-Restrained specimens under 20 MPa.

while in real structures, this period is from 10 to 50 years. This indicates that visual inspection would not capture defects in structures that might have lost, in some areas, up to 25% of the strength before about 5–25 years. Also by looking at the CDFs for crack volumes, it can be noticed that most of the crack volume is contributed by the smaller cracks. For example, crack openings greater than 100 μm only contribute 5% in crack volume which emphasizes more on the danger of only using visual inspection as it is hard to estimate the amount of cracking if only 5% of it is visible. Another phenomena can be interpreted from comparing crack opening CDF with crack volume CDF at each time. At 90 days which correspond to 20% of the maximum expansion, crack volume CDF is very close to crack opening CDF, which suggests a linear relationship between the two. Cracks with opening up to the average of 12.4 μm contribute about 43% of crack volume. At 180 days, corresponding to 60% of maximum expansion, crack volume CDF is deviating more from the crack opening CDF, showing more volume contribution from larger crack openings. Here, cracks with opening up to the average of 15 μm contribute about 30% of crack volume. The same trends are shown with increasing of cracking. At 450 days, crack volume CDF is clearly distinct from crack opening CDF, showing even more volume contribution from larger crack openings. In this case, cracks with opening up to the average of 17.5 μm contribute about 27% of crack volume.

After model calibration, model validation was performed by simulating all the remaining data from Ref. [26] and by keeping all parameters unchanged. Results and discussion of the validation are presented in the following sections.

5.1.3. Effect of applied load on reactive unrestrained specimens

In addition to the free expansion case, Multon and Toutlemonde [26] tested unrestrained specimens subjected to two levels of axial stress, σ_a = 10 and 20 MPa. Comparison between numerical prediction and experimental results is shown in Fig. 2b, and c, for the axial strain, and Fig. 3b, and c, for the radial strain. For axial and radial strain, the Simulated 2 and 3 curves agree very well with the experimental data. The simulated 2 curve matches the experiments slightly better, especially as far as the radial response is concerned. This suggests that for the unrestrained specimens the drying shrinkage assumption is closer to the reality and some loss of sealing could have occurred during the test period. Furthermore, analysis of the Simulated 1 curves, indicates that when an axial load is applied, most of the ASR induced expansion occurs in the radial direction. The axial ASR expansion is close to zero and it even reverses to a contraction for the 20 MPa case. This result shows clearly the ability of the model to redirect the ASR expansion based on stress state, without postulating any effect of stress state on gel formation and expansion but solely through the correct simulation of meso-scale cracking. Obviously these results do not disprove the possibility that both gel formation and water imbibition could be reduced or even stopped for very high levels of confined compression.

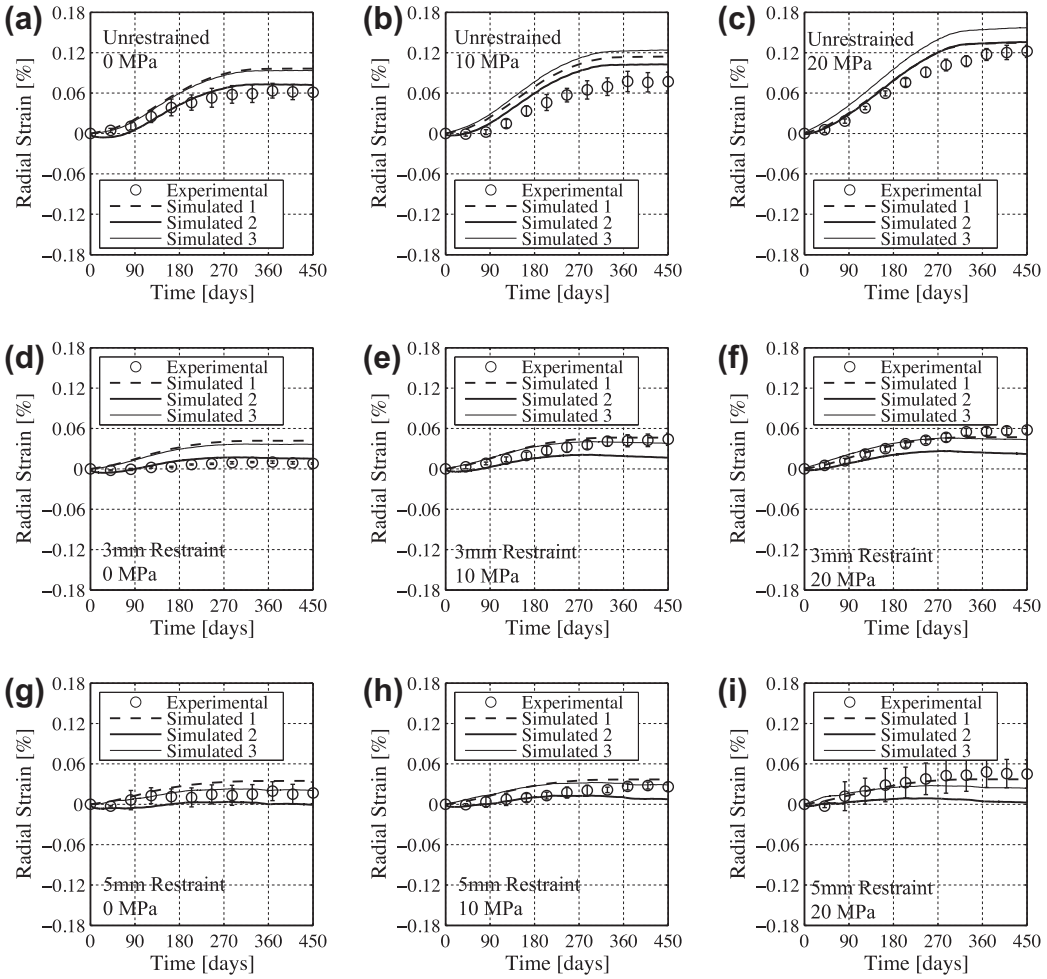

Fig. 3. Radial strain evolution for: (a) Unrestrained specimens under 0 MPa, (b) Unrestrained specimens under 10 MPa, (c) Unrestrained specimens under 20 MPa, (d) 3-mm-Restrained specimens under 0 MPa, (e) 3-mm-Restrained specimens under 10 MPa, (f) 3-mm-Restrained specimens under 20 MPa, (g) 5-mm-Restrained specimens under 0 MPa, (h) 5-mm-Restrained specimens under 10 MPa, and (i) 5-mm-Restrained specimens under 20 MPa.

5.1.4. ASR effect on restrained specimens

This section presents the simulation of experimental data relevant to two sets of laterally restrained specimens subject to ASR [26]. The lateral restraints were composed of a series of 10-mm-high steel rings devised to prevent restraining in the axial direction. Two different steel ring thicknesses were used, namely 3 mm and 5 mm. Both cases were tested under no axial load; as well as with 10 MPa and with 20 MPa axial compressive stresses. In the numerical simulations, the effect of the steel rings was modeled by placing the LDPM specimens in contact with a frictionless cylindrical container modeled through elastic quadratic shell elements. Comparison between numerical predictions and experimental results is shown in Fig. 2d through i for axial strains; and Fig. 3d through i for radial strains.

Due to the effect of confinement the general trend with and without axial stress is an increase of the axial expansion and a significant reduction of the radial one (see Simulated 1 curves). However, when the axial stress is applied, creep and shrinkage dominate the deformation in the axial direction and the increased axial expansion is actually reflected in a reduced overall shortening (see Simulated 2 and 3 curves). Overall the agreement between the experimental data and the numerical prediction is remarkable. In this case, however, the Simulated 3 prediction (with only autogenous shrinkage) tends to be slightly better than the Simulated 2. This is reasonable because, in the experiments, the presence of the tightly spaced metal rings certainly helped keep the sealing in place preventing the decrease of relative humidity discussed earlier in this paper in relation to the unrestrained specimens.

5.1.5. Discussion of expansion transfer mechanism

Different stress states lead to a distinctly different macroscopic expansive behavior of concrete specimens subject to ASR. The general trend is that, when a compressive stress is applied in one direction, the ASR expansion reduces in that direction while, at the same time, it increases in the direction orthogonal to it. Some authors [21] suggested a direct dependence of gel production and water imbibtion on applied stress. This concept, which certainly has a strong foundation in the known dependence of many chemical reactions on stress state [85], cannot explain, however, the additional expansion in the transverse direction. This motivated some other authors [26,80,86] to postulate the existence of the so-called "gel transfer mechanism" according to which ASR is not stress dependent (at least at the level of stress of typical applications) and the expansion transfer is explained through ASR gel migration under the effect of the applied stress. In other words, it is assumed that compressive stresses "squeeze out" gel from the pores of concrete making it to redirect in the more favorable direction transverse to the applied load. This interpretation is highly questionable in the case of undamaged concrete, which is characterized by a complex pore structure and a very stiff solid skeleton. In support to this statement and contrarily to the behavior of other porous materials, experimental data [87] have clearly shown that compressive stresses have negligible or no effect on even moisture transfer. It is possible, however, that gel migration occurs in the case of damaged concrete in which open cracks provide enough room for the gel to be released in. In such a scenario, however, it is likely that pressure build up would be minimal and gel expansion due to water imbibition would be accommodated in the empty space provided by the crack, leading to no additional macroscopic expansion.

In the present study the aforementioned "gel redirection" mechanism is not adopted and, expansion transfer is explained through the redirection of cracking at the meso-scale. This is one of the unique advantages of implementing the ASR model within the LDPM framework that is capable of reproducing the heterogeneous character of concrete behavior as well as crack patterns reported typically in experiments [2,8].

Fig. 4c show the random and heterogeneous nature of crack patterns in simulated specimens subjected to ASR. The cracks shown represent cracks with openings larger 10 μm. The maximum calcu-

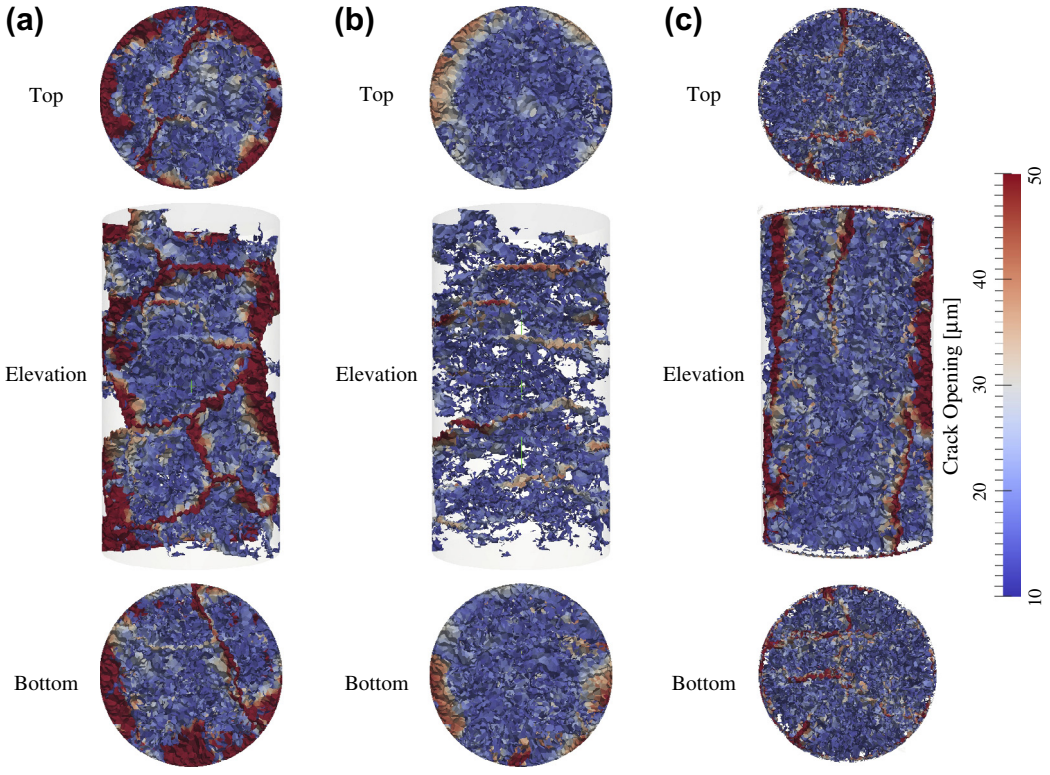

Fig. 4. Crack patterns simulated in one specimen for (a) free expansion case, (b) 0 MPa and 5-mm-restraint case, and (c) 20 MPa unrestrained case.

lated crack opening is about 180 μm, which matches well the crack width range (between 9 μm and 200 μm) reported in similar experimental data [1].

Fig. 4a shows the crack pattern distribution of one simulated specimen under unrestrained free expansion. As one can see, there is no preferential orientation in the crack distribution. Top and bottom views show cracking in radial and circumferential direction and elevation shows both radial and axial crack propagation. For the same specimen (same particle position and size), Fig. 4b shows the calculated crack pattern for the case of passive restraining with 5-mm restraint under no axial loading. The simulations predict a clear redirection of cracks in the radial direction: the top and bottom views do not show radial cracks and elevation view only shows almost horizontally aligned cracks. Opposite situation arises if, again, the same specimen is subjected to axial load and without restraint as shown in Fig. 4c for the 20 MPa case. This figure shows clearly the redirection of cracks in the vertical direction, parallel to the applied load. Top and bottom views show cracking in radial direction and the elevated view shows clearly vertical crack propagation and virtual not cracks orthogonal to the applied compressive load. For all cases, similar type of crack patterns were reported in the literature by other authors [2,8].

Additional insight on the ASR behavior of concrete can be gained by decoupling the calculated ASR expansion in two separate components: one due to gel expansion and one due to cracking. The evolution in time of these components is shown in Fig. 5a–d; for free-expansion, unrestrained expansion with axial load (20 MPa), restrained (with 5-mm rings) expansion with no applied axial load, and restrained (with 5-mm rings) expansion with applied axial load (20 MPa), respectively. Macroscopically, these four cases correspond to stress-free, uniaxial, biaxial, and triaxial compressive stress states. According to the formulation, the results show the volumetric expansion due to the gel to be exactly the same and basically coinciding with the total volumetric strain up to 58.3, 6.8, 79.3, and 122 days, for the four cases, respectively. These times correspond to the elastic expansion part. Here it should be noticed that for all cases except the loaded case with no restraints, cracking starts after a comparably longer period to the loaded case. This is because 20 MPa axial load with no restraints causes initial cracking inside the specimen which makes it much easier for the ASR imposed gel strain to drive the already present cracks to progress in the meso-structure. All other cases follow the logic trend of delayed cracking with higher confinement. Afterwards, cracking develops in a very distinct manner depending on the macroscopic stress-state. At 450 days, the amount of expansion due to cracking decreases from about 2.5 times the gel expansion for the specimen under free expansion down to 2.25 times gel expansion for the uniaxial stress state of the unrestrained case

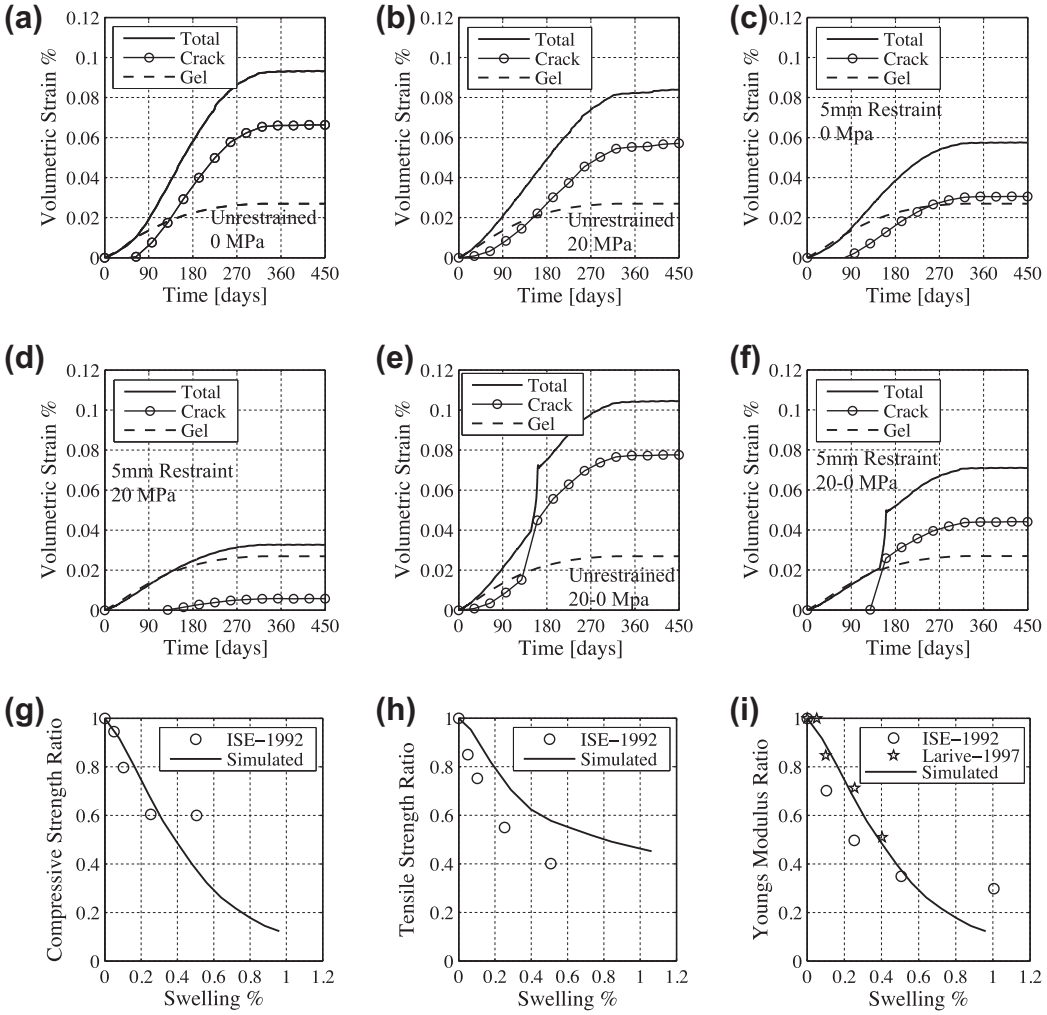

Fig. 5. Volumetric strain components for: (a) free expansion case; (b) 20 MPa case; (c) 0 MPa and 5-mm-restraint case; (d) 20 MPa and 5-mm-restraint case; (e) unrestrained 20 MPa case with unloading after 150 days; (f) 20 MPa 5-mm-restraint case with unloading after 150 days. Effect of ASR on: (g) compressive strength; (h) tensile strength; and (i) tangent elastic modulus.

with 20 MPa axial loading. With more confinement, cracking expansion goes down to 1.14 times gel expansion for the biaxial stress state of the restrained case with 5 mm rings, becoming almost negligible (about 0.3 of gel expansion) for the triaxial stress state. This reduction is obviously due to crack closure induced by the applied compressive stresses. The LDPM formulation automatically captures this effect without the need of postulating a phenomenological dependence of ASR damage on stress state as done in all available approaches [62,51–55] based on continuum mechanics and not accounting for material heterogeneity.

Fig. 5e and f show the evolution of cracking and gel expansion in two additional cases: (1) the unrestrained case with axial load (20 MPa) in the axial direction in which the load is removed after 150 days of ASR; and (2) the restrained case (with 5-mm rings) with axial load (20 MPa) in the axial direction in which, axial load is removed after 150 days of ASR. These two situations are meant to mimic the practical situations in which concrete cores are extracted from ASR affected structures to assess the level of deterioration. The time 150 days corresponds to almost 50% ASR expansion in the free expansion case. In Fig. 5e, the release of load causes a sudden jump in the crack volume, this causes more cracking up to 0.0776% compared to the free expansion case of 0.0663% (Fig. 5a). Fig. 5f shows the same trend of higher crack volume reaching 0.0441% compared to 0.0306% for the same final case (Fig. 5c). Both cases represent clearly what is reported about cored specimens, which degrade significantly if left in the laboratory for some time after coring and before testing. During this time, the entrained ASR gel pressure cracks the meso-structure rapidly as the confining pressure is released.

5.2. Simulation of effect of ASR on concrete strength

The deterioration of mechanical properties of concrete due to ASR has been addressed by many authors [1,11,8,88,62]. Here, the experimental data reported in Ref. [62] were used for validation. Due to lack of information about the characteristics of concrete used and the expansion time histories (only reduction of mechanical properties versus swelling is reported), the same concrete properties reported in Ref. [26] were used. Numerical simulations were performed using exactly the same LDPM parameters reported in Section 5.1.1. However, to cover up to 1% swelling (volumetric change corresponding to 0.33% volumetric strain) which is about 4 times that of free expansion in [26] (see Fig. 1f), two of the ASR model parameters reported in Section 5.1.2 were changed to: $a_{s0} = 0.739 \times 10^{-10}$ m^2/day and $C_i^0 = 3.599 \times 10^{-14}$ m^2/day. Fig. 5g–i shows the reduction in concrete mechanical properties versus percentage of swelling. For each property, at each simulated swelling value, the response average of three different geometries is divided by the corresponding simulated value of the control specimens. Fig. 5g shows the effect of ASR swelling on concrete compression strength f_c' and compares it with the experimental data of ISE 1992 (The Institute of Structural Engineers) reported in Ref. [62]. It is clear from the first portion of the curve that simulations are in excellent agreement with experimental data. Also, for the remaining part of the simulated curve, the curve tends to flatten. Fig. 5h discusses tensile strength f_t'. Here, the model overestimates the experimental results, suggesting less reduction in tensile strength than the reported experimental data. It is important to note here that the simulations are relevant to splitting tests while, type of test used in experiments was not mentioned. Additionally, simulations are referenced to concrete with 3.2 MPa of tensile strength while also the concrete tensile strength of the experimental data was not available. Overall, the model could capture the trend also in tension. Finally, Fig. 5i shows the reduction of elastic Modulus from numerical simulation along with experimental data of ISE 1992 and data from Larive's PhD thesis [62]. Simulations show excellent agreement with experimental data for up to 0.6% swelling with underestimation of the values for higher swelling. It should be noted that at such high swelling value, concrete is extensively cracked with very large loss of strength that would clearly induce very high scatter in strength and stiffness measurements. Additionally for such a level of damage, it is not easy to define a clear tangent modulus that accurately describe concrete elastic properties because the linear elastic behavior at such a level is lost due to excessive cracking. In addition, it must also be observed that even the size of specimens was not reported leaving size-effect as a very crucial factor not accounted for in the simulations. So, generally speaking, the model for a given level of swelling can predict with satisfactory accuracy both the reductions in concrete properties as well as the reduction rate up to a very high swelling of 1%.

5.3. Alkali content effect on ASR expansion

In this section experimental data from Refs. [89,35] are used to demonstrate the ability of the formulated model to capture the effect of alkali content on the ASR expansion. For the first data set [89], the free expansions of sealed concrete prisms (75 mm × 75 mm × 265 mm) were recorded in axial direction over 730 days, the experiments were conducted according to CSA A23.2 Test 14A [18] (equivalent to ASTM C 1293 [19]), the reactive grain size distribution given by author was 1 part of fine aggregate to 2 parts of coarse aggregate. More specifically, the distribution was: 1/3 of aggregate particles between 4.75 and 9.5 mm, 1/3 between 9.5 and 12.5 mm and the last third between 12.5 and 19.0 mm. The experimental as well as simulated specimen grain size distributions are shown in Fig. 6a. LDPM geometry generation was carried out with following parameters: minimum aggregate size, $d_0 = 4.75$ mm; maximum aggregate size, $d_a = 19$ mm; fuller curve exponent, $n_F = 0.55$; and the following mix composition: cement content, $c = 420$ kg/m^3; water-to-cement ratio, $w/c = 0.45$; aggregate-to-cement ratio, $a/c = 4.25$.

For the second data set in Ref. [35], the free expansions of sealed concrete prisms (75 mm × 75 mm × 250 mm) using Siltstone aggregate at 38°C were recorded in axial direction over 730 days after curing in moist air for 7 days, aggregate consisted of a mixture of 2 parts coarse aggregate (20–5 mm) to 1 part fine aggregate. The distribution of coarse aggregate portions was not mentioned so it was assumed to be equally distributed into three equal portions (typically recommended for ASR prism tests). The experimental as well as simulated specimen grain size distributions are shown in Fig. 6d. LDPM geometry generation was obtained with following parameters: minimum aggregate size, $d_0 = 5$ mm; maximum aggregate size, $d_a = 20$ mm; fuller curve exponent, $n_F = 0.6$; and the following mix composition: cement content, $c = 400$ kg/m^3; water-to-cement ratio, $w/c = 0.5$; aggregate-to-cement ratio, $a/c = 4.6$. For both sets, no data about concrete mechanical properties was available, so the same LDPM parameters used in Section 5.1.1 were used.

For the first data set [89], the experimental data show a bilinear relation between maximum expansion and alkali content (Fig. 6c). By fitting the experimental data assuming the maximum expansion to be 0.25%, the saturation alkali content c_a^1 was found to be 4.37 kg/m^3. Setting $\kappa_a = 1$, the ASR model parameters were calibrated using the highest experimental curve at 5.25 kg/m^3. Afterwards, the threshold Alkali content c_a^0, was identified by fitting the maximum expansion for $c_a = 3.15$ kg/m^3 and was found to be 2.70 kg/ m^3. Calibrated ASR parameters were: $a_{s0} = 0.518 \times 10^{-10}$ m^2/day, $C_i^0 = 32.5 \times 10^{-14}$ m^2/day, $\eta = 439{,}540$ kg^{-1}.

The second data set [35] did not show the complete range of alkali content so it was assumed that the saturation alkali content c_a^1, was the largest reported one (7.0 kg/m^3). Following the same pro-

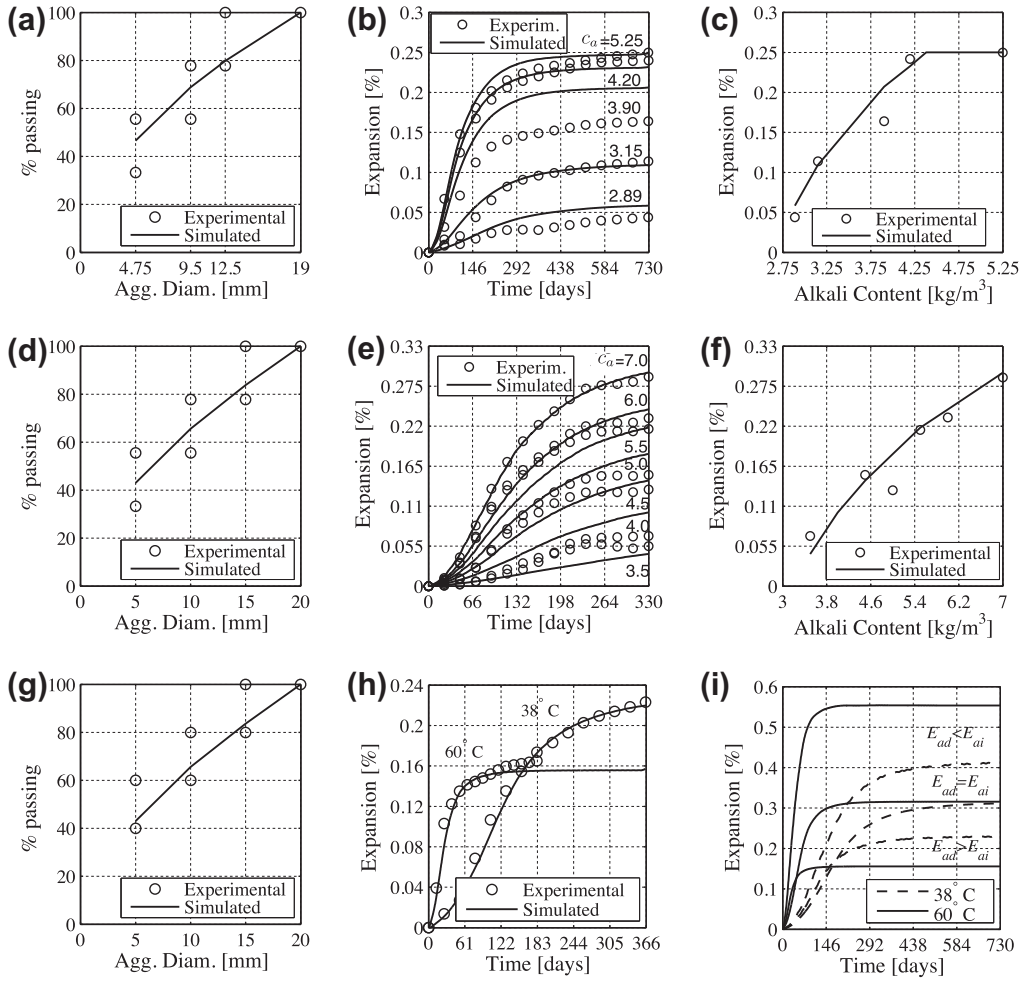

Fig. 6. Simulated and experimental sieve curve for Data in (a) Ref. [89], and (d) Ref. [35]. Effect of alkali contents on expansions evolution for data from (b) Ref. [89], and (e) Ref. [35]. Maximum expansion versus alkali content for (c) Ref. [89] and (f) Ref. [35], (g) Simulated and experimental sieve curve for data from Ref. [90], (h) Simulation of Temperature effect Results at 38 °C and 60 °C, and (i) Relation between activation energies.

cedure, ASR model parameters were calibrated based on the largest curve at 7.00 kg/m^3, while setting $\kappa_a = 1$, then the alkali content threshold c_a^0 was calibrated to match the maximum expansion of the curve at $c_a = 4.5$ kg/m^3 and was found to be 3.15 kg/m^3. Calibrated ASR parameters were: $a_{s0} = 0.333 \times 10^{-10}$ m^2/day, $C_i^0 = 39.701 \times 10^{-14}$ m^2/day, $\eta = 460{,}680$ kg^{-1}.

After calibration, while keeping all parameters fixed, the other alkali contents were simulated and the results are shown in Fig. 6b, c, e and f. Fig. 6b and e show both experimental and simulated expansion curves with different alkali contents while Fig. 6c and f show the expansion maximum values of both experimental and simulated data. The following observations can be made from the results: (1) for both sets, the model predicts very well the expansion maximum values for different alkali contents (see Fig. 6c and f); (2) a slight deviation from the linear assumption is noticed in the unsaturated part $c_a < c_a^1$, this is due to the fact that at lower gel strains, less cracking is produced while increasing the gel volume results in more cracking and their relation is clearly nonlinear; (3) at different alkali contents, the model matches very well the experimental expansion history (Fig. 6b and e) considering the scatter of experimental data; (4) at low alkali contents, the experimental data was not so accurate as the reported expansion at $c_a = 4.0$ kg/m^3 was slightly less than the reported value at $c_a = 3.5$ kg/m^3 for the second set as shown in Fig. 6e, also at $c_a = 2.89$ kg/m^3 for the first data set, the evolution with time shows slight drop in the middle, this can be just due to experimental scatter as well as the very low amount of expansion to be reported which allows for higher measurement error.

5.4. Simulation of effect of temperature change

This section investigates the effect of temperature on ASR expansion. The relevant data set is the expansion tests of Spratt aggregate reported in Ref. [90]. The free expansions of concrete prisms (75 mm × 75 mm × 300 mm) were recorded in axial direction over 183 days at 60 °C and 366 days at 38 °C. Curing for the first 24hours was done in molds covered with plastic sheets and wet burlap. Then the specimens were stripped, wrapped in wet cloth towels and stored in plastic bags at 23 °C overnight. In the morning, initial measurements were taken and specimens were then maintained at relevant test temperature (38 °C or 60 °C) with RH > 95% for the rest of the test period. Concrete grain size distribution for these experiments was designed to be according to the Canadian standard CSA3A23.2-14A [18] as stated by the author. Thus coarse aggregate was assumed to be evenly divided into three equal portions and the ratio between fine and coarse aggregate was 0.4 to 0.6 by weight. Sieve curve of both experimental and simulated specimens is shown in Fig. 6g. LDPM parameters used in geometry generation were: minimum aggregate size, $d_0 = 5$ mm; maximum aggregate size, $d_a = 20$ mm; fuller curve

exponent, $n_F = 0.6$; cement content, $c = 420$ kg/m^3; water-to-cement ratio, $w/c = 0.43$; aggregate-to-cement ratio, $a/c = 4.2667$. No concrete strength information was reported, so the LDPM parameters used in Section 5.1.1 were used since concrete composition was somewhat similar.

In the experiments, only two temperatures, 38 °C and 60 °C, were considered which were enough for the calibration of the activation energies for gel formation and water imbibition but did not allow a complete validation of the model. The parameter identification was performed by assuming as reference temperature $T_0 = 23$ °C = 296 K and resulted in the following parameters: $a_{s0} = 0.0801 \times 10^{-10}$ m^2/day, $C_i^0 = 12.646 \times 10^{-14}$ m^2/day, $\eta = 943{,}449$ kg^{-1}, $E_{ad} = 45{,}206$ J/mole, $E_{ai} = 70{,}748$ J/mole.

The obtained best fitting of the experimental expansion curves is shown in Fig. 6h for the cases at 38 °C and 60 °C, respectively. Very accurate matching can be seen between experimental data and simulated results. By increasing the temperature to 60 °C (Fig. 6h), the model is able to capture the complete trend of the ASR expansion, namely the higher expansion rate at higher temperature as well as the change in maximum expansion value from 0.2202% after 366 days at 38 °C, to 0.1557% after 183 days at 60 °C. To capture the difference in maximum expansion for different temperature, the two activation energies are needed. While the two activation energies, E_{ad} and E_{ai}, are not necessarily equal, additional analysis was done to show the effect of their relative values. Fig. 6i shows three different cases in which, the two activation energies are equal ($E_{ad} = E_{ai} = 45{,}206$ J/mole), in this case, both temperatures lead to the same asymptotic expansion of 0.316%. The second case is when $E_{ad} = 70{,}748$ J/mole and $E_{ai} = 45{,}206$ J/mole, here the higher temperature has lower asymptotic expansion (0.1557% at 60 °C compared to 0.2308% at 38 °C. The third case is the opposite of the second, where $E_{ad} = 45{,}206$ J/mole and $E_{ai} = 70{,}748$ J/mole, here the higher temperature has higher asymptotic expansion (0.554% at 60 °C compared to 0.4155% at 38 °C. With this formulation, ASR-LDPM can capture the correct effect of temperature on both, expansion rate and maximum expansion values.

6. Conclusions

This paper presents the formulation of a novel approach, entitled ASR-LDPM, to simulate the effect of ASR on concrete structures. ASR-LDPM implements, within the mesoscale framework of LDPM, a model describing ASR gel formation and expansion at the level of each individual aggregate particle. ASR-LDPM was calibrated and validated with reference to several sets of experimental data dealing with ASR effects on concrete under a variety of different loading and environmental conditions with the limitation to saturated conditions. Based on the obtained results, the following conclusions can be drawn:

1. ASR-LDPM can predict accurately free and restrained ASR-induced expansion under various loading conditions and can reproduce realistic crack patterns.
2. ASR-LDPM is the only model available in the literature that distinguishes between the volume expansion directly associated with ASR gel and the one associated with cracking. This is a unique feature allowing it to precisely predict expansion anisotropy as well as strength and stiffness reduction.
3. The amount and distribution of cracking varies upon the applied macroscopic stress state, leading to change in the volumetric expansion even if no direct effect of stress on gel formation and water imbibition is postulated. ASR-LDPM explains the experimentally observed "expansion transfer" as redirection of cracking rather than redirection of gel expansion as advocated by other researchers in the literature.
4. ASR-LDPM predicts material deterioration directly without the need of phenomenological laws relating gel volume and expansion to concrete mechanical properties.
5. Significant material deterioration associated with not negligible strength reduction is predicted under free expansion even for crack openings not detectable by naked eye.
6. Confining stresses prevent the evolution of cracking during the evolution of gel expansion. However, cracking develops subsequently if the confining stresses are released. This complicates or even invalidates the destructive evaluation of ASR affected structures.
7. ASR-LDPM is capable of replicating the effect of change in alkali ion concentration which depends on cement type and content and water alkalinity with very good accuracy.
8. Postulating the existence of two separate activation energies, one for gel formation and one for water imbibition, allows simulating correctly the effect of temperature on rate of expansion and maximum expansion.

Acknowledgments

This material is based upon work supported by the Science & Technology Directorate, U.S. Department of Homeland Security, under Award Number 2009-ST-108-001. The views and conclusions contained in this document are those of the authors and should not be interpreted as necessarily representing the official policies, either expressed or implied, of the U.S. Department of Homeland Security.

Appendix A. LDPM costitutive equations

For stresses and strains beyond the elastic limit, LDPM mesocale failure is characterized by three mechanisms as described below.

A.1. Fracture and cohesion due to tension and tension-shear

For tensile loading ($\varepsilon_N > 0$), the fracturing behavior is formulated through an effective strain, $\varepsilon = \sqrt{\varepsilon_N^2 + \alpha(\varepsilon_M^2 + \varepsilon_L^2)}$, and stress, $\sigma = \sqrt{\sigma_N^2 + (\sigma_M + \sigma_L)^2/\alpha}$, which define the normal and shear stresses as $\sigma_N = \varepsilon_N(\sigma/\varepsilon)$; $\sigma_M = \alpha\varepsilon_M(\sigma/\varepsilon)$; $\sigma_L = \alpha\varepsilon_L(\sigma/\varepsilon)$. The effective stress σ is incrementally elastic ($\dot{\sigma} = E_0\dot{\varepsilon}$) and must satisfy the inequality $0 \leqslant \sigma \leqslant \sigma_{bt}(\epsilon,\omega)$ where $\sigma_{bt} = \sigma_0(\omega)\ \exp[-H_0(\omega)\langle\ \varepsilon - \varepsilon_0(\omega)\rangle/\sigma_{0}(\omega)]$, $\langle x\rangle = \max\{x,0\}$, and $\tan(\omega) = \varepsilon_N/\sqrt{\alpha}\varepsilon_T = \sigma_N\sqrt{\alpha}/\sigma_T$. The post peak softening modulus is defined as $H_0(\omega) = H_t(2\omega/\pi)^{n_t}$, where H_t is the softening modulus in pure tension ($\omega = \pi/2$) expressed as $H_t = 2E_0/(l_t/l_e - 1)$; $l_t = 2E_0G_t/\sigma_t^2$; l_e is the length of the tetrahedron edge; and G_t is the mesoscale fracture energy. LDPM provides a smooth transition between pure tension and pure shear ($\omega = 0$) with parabolic variation for strength given by $\sigma_0(\omega) = \sigma_t r_{st}^2\left(-\sin(\omega) + \sqrt{\sin^2(\omega) + 4\alpha\cos^2(\omega)/r_{st}^2}\right)/[2\alpha\cos^2(\omega)]$, where $r_{st} = \sigma_s/\sigma_t$ is the ratio of shear strength to tensile strength.

A.2. Compaction and pore collapse from compression

Normal stresses for compressive loading ($\varepsilon_N < 0$) are computed through the inequality $-\sigma_{bc}(\varepsilon_D,\ \varepsilon_V) \leqslant \sigma_N \leqslant 0$, where σ_{bc} is a strain-dependent boundary function of the volumetric strain, ε_V, and the deviatoric strain, ε_D. Beyond the elastic limit, $-\sigma_{bc}$ models pore collapse as a linear evolution of stress for increasing volumetric strain with stiffness H_c for $-\varepsilon_V \leqslant \varepsilon_{c1} = \kappa_{c0}\,\varepsilon_{c0}$: $\sigma_{bc} = \sigma_{c0} + \langle -\varepsilon_V - -\ \varepsilon_{c0}\rangle H_c(r_{DV})$; $H_c(r_{DV}) = H_{c0}/(1 + \kappa_{c2}\ \langle\ r_{DV} - \kappa_{c1}\rangle)$; σ_{c0} is the mesoscale compressive yield stress; and κ_{c1}, κ_{c2} are material

parameters. Compaction and rehardening occur beyond pore collapse ($-\varepsilon_V \geqslant \varepsilon_{c1}$). In this case one has $\sigma_{bc} = \sigma_{c1}(r_{DV})\exp[(-\varepsilon_V - \varepsilon_{c1})H_c(r_{DV})/\sigma_{c1}(r_{DV})]$ and $\sigma_{c1}(r_{DV}) = \sigma_{c0} + (\varepsilon_{c1} - \varepsilon_{c0})H_c(r_{DV})$.

A.3. Friction due to compression-shear

The incremental shear stresses are computed as $\dot{\sigma}_M = E_T(\dot{\varepsilon}_M - \dot{\varepsilon}_M^p)$ and $\dot{\sigma}_L = E_T(\dot{\varepsilon}_L - \dot{\varepsilon}_L^p)$, where $\dot{\varepsilon}_M^p = \dot{\lambda}\partial\varphi/\partial\sigma_M, \dot{\varepsilon}_L^p = \dot{\lambda}\partial\varphi/\partial\sigma_L$, and λ is the plastic multiplier with loading–unloading conditions $\varphi\dot{\lambda} \leqslant 0$ and $\dot{\lambda} \geqslant 0$. The plastic potential is defined as $\varphi = \sqrt{\sigma_M^2 + \sigma_L^2} - \sigma_{bs}(\sigma_N)$, where the nonlinear frictional law for the shear strength is assumed to be $\sigma_{bs} = \sigma_s + (\mu_0 - \mu_\infty)\sigma_{N0}[1 - \exp(\sigma_N/\sigma_{N0})] - \mu_\infty\sigma_N$; σ_{N0} is the transitional normal stress; μ_0 and μ_∞ are the initial and final internal friction coefficients.

References

[1] Giaccio G, Zerbino R, Ponce J, Batic OR. Mechanical behavior of concretes damaged by alkali–silica reaction. Cem Concr Res 2008;38:993–1004.
[2] Saouma V, Xi Y. Literature review of alkali aggregate reactions in concrete dams. Report cu/sa-xi-2004/001. Department of Civil, Environmental, & Architectural Engineering University of Colorado; 2004.
[3] Stanton TE. Expansion of concrete through reaction between cement and aggregate. Proc Am Soc Civ Eng 1940;66:1781–811.
[4] Hobbs DW. Alkali–silica reaction in concrete. London: Thomas Telford; 1988.
[5] Swamy RN, Al-Asali MM. Engineering properties of concrete affected by alkali–silica reaction. ACI Mater J 1988;85:367–74.
[6] Swamy RN, Al-Asali MM. Effect of alkali–silica reaction on the structural behavior of reinforced concrete beams. ACI Mater J 1989;86:451–9.
[7] Clark LA. Modeling the structural effects of alkali–silica reactions on reinforced concrete. ACI Mater J 1991;88:271–7.
[8] Ahmed T, Burley E, Rigden S, Abu-Taira AI. The effect of alkali reactivity on the mechanical properties of concrete. Constr Build Mater 2003;17(2):123–44.
[9] Fan SF, Hanson JM. Length expansion and cracking of plain and reinforced concrete prisms due to alkali–silica reaction. ACI Mater J 1998;95:480–7.
[10] Monette LJ, Gardner NJ, Grattan-Bellew PE. Residual strength of reinforced concrete beams damaged by alkali–silica reaction – examination of damage rating index method. ACI Mater J 2002;99:42–50.
[11] Multon S, Seignol J-F, Toutlemonde F. Structural behavior of concrete beams affected by alkali–silica reaction. ACI Mater J 2005;102(2):67–76.
[12] Fernandes I, Noronha F, Teles M. Microscopic analysis of alkali-aggregate reaction products in a 50-year-old concrete. Mater Charact 2004;5(2-4):295–306.
[13] Ramyar K, opuroglu O, Andi, Fraaij ALA. Comparison of alkali–silica reaction products of fly-ash- or lithium-salt-bearing mortar under long-term accelerated curing. Cem Concr Res 2004;34(7):1179–83.
[14] Peterson K, Gress D, Vandam T, Sutter L. Crystallized alkali-silica gel in concrete from the late 1890s. Cem Concr Res 2006;36(8):1523–32.
[15] 126094 AC. Standard test method for determining the potential alkali reactivity of combinations of cementious materials and aggregate (accelerated mortar-bar method). Annual Book of ASTM Standards 2002, American Society for Testing and Materials, Philadelphia, PA; 2002.
[16] A23.225A00 C. Detection of alkali-silica reactive aggregate by accelerated expansion of mortar bars. CSA A23.200: Methods of Test for Concrete, Canadian Standards Association, Mississauga.
[17] R TC191-ARP-AAR02. Detection of potential alkali-reactivity of aggregates-the ultra-accelerated mortar-bar test. Mater Struct 2000;33:283–93.
[18] A23. 214A00 C. Potential expansivity of aggregates (procedure for length change due to alkali-aggregate reaction in concrete prisms). CSA A23.200: Methods of Test for Concrete, Canadian Standards Association, Mississauga (ON); 2000. p. 207–16.
[19] 129301 AC. Standard test method for concrete aggregates by determination of length change of concrete due to alkali–silica reaction. Annual Book of ASTM Standards, vol. 04.02 (Concrete and Aggregates), Philadelphia (PA); 2002.
[20] Vivian HE. The effects on mortar expansion of reactive component in the aggregate. Stud Cem–Aggr Reactions, Part 10. CSIRO Bull 1947;256:13–20.
[21] Bažant Z, Steffens A. Mathematical model for kinetics of alkali–silica reaction in concrete. Cem Concr Res 2000;30:419–28.
[22] Suwito A, Jin W, Xi Y, Meyer C. A mathematical model for the pessimum size effect of ASR in concrete. Concr Sci Eng 2002;4(13):23–34.
[23] Multon S, Sellier A, Cyr M. Chemomechanical modeling for prediction of alkali silica reaction (ASR) expansion. Cem Concr Res 2009;39(6):490–500.
[24] Berra M, Mangialardi T, Paolini AE. Rapid evaluation of the threshold alkali level for alkali-reactive siliceous aggregates in concrete. Cem Concr Compos 1999;21(4):325–33.
[25] Smaoui N, Berube M, Fournier B, Bissonnette B, Durand B. Effects of alkali addition on the mechanical properties and durability of concrete. Cem Concr Res 2005;35(2):203–12.
[26] Multon S, Toutlemonde F. Effect of applied stresses on alkali–silica reaction-induced expansions. Cem Concr Res 2006;36:912–20.
[27] Multon S, Cyr M, Sellier A, Leklou N, Petit L. Coupled effects of aggregate size and alkali content on ASR expansion. Cem Concr Res 2008;38(3):350–9.
[28] Puertas F, Palacios M, Gil-Maroto A, Vzquez T. Alkali-aggregate behaviour of alkali-activated slag mortars: effect of aggregate type. Cem Concr Compos 2009;31(5):277–84.
[29] Berra M, Faggiani G, Mangialardi T, Paolini AE. Influence of stress restraint on the expansive behaviour of concrete affected by alkali–silica reaction. Cem Concr Res 2010;40(9):1403–9.
[30] Multon S, Cyr M, Sellier A, Diederich P, Petit L. Effects of aggregate size and alkali content on ASR expansion. Cem Concr Res 2010;40(4):508–16.
[31] Multon S, Toutlemonde F. Effect of moisture conditions and transfers on alkali silica reaction damaged structures. Cem Concr Res 2010;40(6):924–34.
[32] Smaoui N, Bissonnette B, Fournier MABB. Stresses induced by alkalisilica reactivity in prototypes of reinforced concrete columns incorporating various types of reactive aggregates. Can J Civ Eng 2007;34(12):1554–66.
[33] Steffens A, Li K, Coussy O. Aging approach to water effect on alkali–silica reaction degradation of structures. J Eng Mech Mater 2003;129:50–9.
[34] Poyet S, Sellier A, Capra B, Thvenin-Foray G, Torrenti JM, Tournier-Cognon H, et al. Influence of water on alkalisilica reaction: experimental study and numerical simulations. J Mater Civ Eng 2006;18(4):588–96.
[35] Sibbick RG, Page CL. Threshold alkali contents for expansion of concretes containing british aggregates. Cem Concr Res 2000;22:990–4.
[36] Bleszynski RF, Thomas MDA. Microstructural studies of alkali–silica reaction in fly ash concrete immersed in alkaline solutions. Adv Cem Based Mater 1998;7(2):66–78.
[37] Karakurt C, Topu B. Effect of blended cements produced with natural zeolite and industrial by-products on alkali–silica reaction and sulfate resistance of concrete. Constr Build Mater 2011;25(4):1789–95.
[38] Amberg F. Performance of dams affected by expanding concrete. V-0009401EN/1021-R-237; 2011.
[39] Hobbs DW. The alkali–silica reactiona model for predicting expansion in mortar. Mag Concr Res 1981;33(117):208–20.
[40] Groves GW, Zhang X. A dilatation model for the expansion of silica glass/OPC mortars. Cem Concr Res 1990;20(3):453–60.
[41] Furusawa Y, Ohga H, Uomoto T. An analytical study concerning prediction of concrete expansion due to alkali–silica reaction. In: Third international conference on durability of concrete, Nice, France. 75780; 1994.
[42] Meyer C, Baxter S. Use of recycled glass and fly ash for precast concrete. Report NYSERDA 9818 (4292-IABR-IA-96) to New York State Energy Research and Developement Authority, Department of Civil Engineering and Engineering Mechanics, Columbia University; 1998.
[43] Xi Y, Suwito A, Wen X, Meyer C, Jin W. Testing and modeling alkali–silica reaction and the associated expansion of concrete. Mechanics of Quasi-Brittle Materials and Structures. In: Proceedings of international workshop in honor of Prof Z P Bazant 60th birthday. Paris: Hermes Science Publications; 1998.
[44] Xi Y, Jennings HM. Shrinkage of cement paste and concrete modelled by a multiscale effective homogeneous theory. Mater Struct 1997;30(6):329–39.
[45] Fick A. Ueber diffusion. Ann Phys 1855;170(1):59–86.
[46] Bažant ZP, Zi G, Meyer C. Fracture mechanics of ASR in concretes with waste glass particles of different sizes. J Eng Mech 2000;126(3):226–32.
[47] Charlwood RG, Solymar SV, Curtis DD. A review of alkali aggregate reactions in hydroelectric plants and dams. In: Proceedings of the international conference of alkali-aggregate reactions in hydroelectric plants and dams, vol. 129. Fredericton, Canada; 1992.
[48] Thompson G, Charlwood R, Steele R, Curtis D. Mactaquac generating station Intake and spillway remedial measures. In: Proceedings for the eighteenth international congress on large dams, Durban, South Africa. V. 1, Q-68, R.24: 34768; 1994.
[49] Lger P, Ct P, Tinawi R. Finite element analysis of concrete swelling due to alkali-aggregate reactions in dams. Comput Struct 1996;60(4):601–11.
[50] Herrador MF, F M-A, Fernndez-Gago RH. Mechanical behavior model for ASR-affected dam concrete under service load: formulation and verification. Mater Struct 2009;42(2):201–12.
[51] Pietruszczak S. On the mechanical behaviour of concrete subjected to alkali-aggregate reaction. Comput Struct 1996;58(6):1093–7.
[52] Huang M, Pietruszczak S. Numerical analysis of concrete structures subjected to alkali-aggregate reaction. Mech Cohes-Frict Mater 1996;1(4):305–19.
[53] Ulm F, Coussy O, Kefei L, Larive C. Thermo-chemo-mechanics of ASR expansion in concrete structures. J Eng Mech 2000;126(3):233–42.
[54] Farage M, Alves JLD, Fairbairn EMR. Macroscopic model of concrete subjected to alkaliaggregate reaction. Cem Concr Res 2004;34(3):495–505.
[55] Fairbairn EMR, Ribeiro FLB, Lopes LE, Toledo-Filho RD, Silvoso MM. Modelling the structural behaviour of a dam affected by alkali–silica reaction. Commun Numer Methods Eng 2005;22(1):1–12.
[56] Larive C. Apports Combin'es de lExperimentation et de la Modlisation la Comprehension del Alcali-Raction et de ses Effets Mcaniques. Dissertation for the Doctoral Degree, Laboratoire Central des Ponts et Chausses, Paris (in France); 1998.
[57] Saouma V, Perotti L. Constitutive model for alkali-aggregate reactions. ACI Mater J 2006;103:194–202.
[58] Multon S, Seignol JF, Toutlemonde F. Chemo-mechanical assessment of beams damaged by alkali–silica reaction. J Mater Civ Eng 2006;18(4):500–9.

[59] Comi C, Fedele R, Perego U. A chemo-thermo-damage model for the analysis of concrete dams affected by alkali–silica reaction. Mech Mater 2009;41(3):210–30.
[60] Comi C, Perego U. Anisotropic damage model for concrete affected by alkali-aggregate reaction. Int J Damage Mech 2011;20(4):598–617.
[61] Poyet S, Sellier A, Capra B, Foray G, Torrenti JM, Cognon H, et al. Chemical modelling of alkali silica reaction: influence of the reactive aggregate size distribution. Mater Struct 2007;40(2):229–39.
[62] Capra B, Sellier A. Orthotropic modelling of alkali-aggregate reaction in concrete structures: numerical simulations. Mech Mater J 2003;35: 817–30.
[63] Pan J, Feng Y, Wang J, Sun Q, Zhang C, Owen D. Front Struct Civ Eng 2012;6(1):1–18.
[64] Comby-Peyrot I, Bernard F, Bouchard PO, Bay F, Garcia-Diaz E. Development and validation of a 3D computational tool to describe concrete behaviour at mesoscale. Application to the alkali–silica reaction. Comput Mater Sci 2009;46(4):1163–77.
[65] Dunant CF, Scrivener KL. Micro-mechanical modelling of alkali-silica-reaction-induced degradation using the AMIE framework. Cem Concr Res 2010;40(4):517–25.
[66] Shin JH, Struble LJ, Kirkpatrick RJ. Modeling alkali–silica reaction using image analysis and finite element analysis. In: Proceedings of the 6th international symposium on cement and concrete and canmet/aci international symposium on concrete technology for sustainable development, vol. 3; 2006. p. 1669–75.
[67] Shin Jh. Modeling alkali–silica reaction using image analysis and finite element analysis, DissertationTip, University of Illinois at Urbana-Champaign; 2009.
[68] Cusatis G, Pelessone D, Mencarelli A. Lattice discrete particle model (LDPM) for concrete failure behavior of concrete. I: Theory. Cem Concr Compos 2011;33(9):881–90.
[69] Cusatis G, Mencarelli A, Pelessone D, Baylot J. Lattice discrete particle model (LDPM) for failure behavior of concrete. II: Calibration and validation. Cem Concr Compos 2011;33(9):891–905.
[70] Poole AB. Introduction to alkali-aggregate reaction in concrete. In: Swamy RN, editor. The alkali–silica reaction in concrete. New York: Van Nostrand Reinhold; 1992. p. 1–28.
[71] Dron R, Brivot F. Thermodynamic and kinetic approach to the alkali–silica reaction: Part 1. Cem Concr Res 1992;22(5):941–8.
[72] Dron R, Brivot F. Thermodynamic and kinetic approach to the alkali–silica reaction: Part 2. Cem Concr Res 1993;23(1):93–103.
[73] Luzio GD, Cusatis G. Hygro-thermo-chemical modeling of high performance concrete. I: Theory. Cem Concr Compos 2009;31(5):301–8.
[74] Castro N, Sorensen BE, Broekmans MA. Assessment of individual ASR-Agregate particles by XRD. In: Proceedings of the 10th international congress for applied mineralogy (ICAM); 2011. p. 95–102. http://dx.doi.org/10.1007/978-3-642-27682-8_13.
[75] Dron R, Brivot F. Solid–liquid equilibria in K–C–S–H/H_2O systems. In: Proceedings of 10th international conference on alkali-aggregate reaction in concrete, Melbourne.
[76] Dron R, Brivot F, Chaussadent T. Mechanism of the alkali–silica reaction. In: 10th International conference on the chemistry of cement, Gothenburg, Sweden, vol. 4.
[77] Bažant Z, Najjar L. Nonlinear water diffusion in nonsaturated concrete. Mater Struct 1972;5(25):3–20.
[78] Jooss M, Reinhardt H. Permeability and diffusivity of concrete as function of temperature. Cem Concr Res 2002;32(9):1497–504.
[79] Powers T, Steinour H. An interpretation of some published researches on the alkali-aggregate reaction. J Am Concr Inst (Proc) 1955;55:497–516. and 785–812.
[80] Larive C, Laplaud A, Joly M. Behavior of AAR-affected concrete: experimental data. In: Proc 10th int conf AAR, Melbourne, Australia; 1996. p. 670–677.
[81] Multon S, Leclainche G, Bourdarot E, Toutlemonde F. Alkali-silicareaction in specimens under multi-axial mechanical stresses. In: Proc 4th int conf CONSEC'04, Seoul, Korea; 2004. p. 2004–11.
[82] Pelessone D. MARS: modeling and analysis of the response of structures – user's manual, ES3, Beach (CA), USA; 2009.
[83] Muller H, Hillsdorf H. CEB Bulletin d information, No. 199, evaluation of the time dependent behavior of concrete, summary report on the work of general task group 9; 1990. p. 290.
[84] Bažant Z, Baweja S. Creep and shrinkage prediction model for analysis and design of concrete structures, the Adam Neville symposium, SP-194. Akthem Al-Manaseer; 2000. p. 1–83.
[85] Treptow RS. Le Chtelier's principle: a reexamination and method of graphic illustration. J Chem Educ 1980;57(6):417–20.
[86] Ahmed T, Burley E, Rigden S. The effect of alkali–silica reaction on the fatigue behaviour of plain concrete tested in compression, indirect tension and flexure. Mag Concr Res 1999;51(6):375–90.
[87] Bažant ZP. Mathematical modeling of creep and shrinkage of concrete. Chichester: John Wiley and Sons; 1988.
[88] Marzouk H, Langdon S. The effect of alkali-aggregate reactivity on the mechanical properties of high and normal strength concrete. Cem Concr Compos 2003;25:549–56.
[89] Shehata MH, Thomas MD. The effect of fly ash composition on the expansion of concrete due to alkali–silica reaction. Cem Concr Res 2000;30:1063–72.
[90] Fournier B, Chevrier R, de Grosbois M, Lisella R, Folliard K, Ideker J, et al. The accelerated concrete prism test (60 °C): variability of the test method and proposed expansion limits. In: Proc 12th international conference on alkali-aggregate reaction in concrete, vol. 1. Beijing, China; 2004. p. 314–23.
[91] Schauffert EA, Cusatis G, Pelessone D, O'Daniel J, Baylot J. Lattice Discrete Particle Model for Fiber Reinforced Concrete (LDPM-F): II Tensile Fracturing and Multiaxial Loading Behavior. ASCE Journal of Engineering Mechanics 2012;138(7):834–41.
[92] Schauffert EA, Cusatis G. Lattice Discrete Particle Model for Fiber Reinforced Concrete (LDPM-F): I Theory. ASCE Journal of Engineering Mechanics 2012;138(7):826–33.
[93] Di Luzio G, Cusatis G. Hygro-Thermo-Chemical Modeling of High Performance Concrete. II: Calibration and Validation. Cement and Concrete Composites 2009;31(5):309–24.